PHYSICAL REVIEW D **84,** 054504 (2011)

Staggered fermions, zero modes, and flavor-singlet mesons

Gordon C. Donald,[1,*] Christine T. H. Davies,[1,†] Eduardo Follana,[2,‡] and Andreas S. Kronfeld[3,§]

(HPQCD and Fermilab Lattice Collaborations)

[1]*SUPA, School of Physics and Astronomy, University of Glasgow, Glasgow G12 8QQ, United Kingdom*
[2]*Departamento de Física Teórica, Universidad de Zaragoza, Cl. Pedro Cerbuna 12, E-50009 Zaragoza, Spain*
[3]*Theoretical Physics Department, Fermi National Accelerator Laboratory, Batavia, Illinois 60510-5011, USA*
(Received 24 June 2011; published 12 September 2011)

We examine the taste structure of eigenvectors of the staggered-fermion Dirac operator. We derive a set of conditions on the eigenvectors of modes with small eigenvalues (near-zero modes), such that staggered fermions reproduce the 't Hooft vertex in the continuum limit. We also show that, assuming these conditions, the correlators of flavor-singlet mesons are free of contributions singular in $1/m$, where m is the quark mass. This conclusion holds also when a single flavor of sea quark is represented by the fourth root of the staggered-fermion determinant. We then test numerically, using the highly improved staggered-quark action, whether these conditions hold on realistic lattice gauge fields. We find that the needed structure does indeed emerge.

DOI: 10.1103/PhysRevD.84.054504 PACS numbers: 11.15.Ha, 11.30.Hv, 11.30.Rd, 12.38.Gc

I. INTRODUCTION

Lattice QCD has made several notable strides over the past decade. A wide variety of calculations with $2 + 1$ flavors of sea quarks (corresponding to up, down, and strange) have been found to agree with experimental measurements within $\sim 2\%$ [1]. Charmed-meson decay constants [2], semileptonic form factors [3], and the masses of the B_c [4] and η_b [5] mesons have been computed before being confirmed by measurements from experiments. Calculations at nonzero temperature have shown that QCD possesses not a first-order phase transition but a smooth crossover [6], with implications for heavy-ion collisions and a cooling universe. Some of the most precise determinations of the strong coupling α_s [7], quark masses [8], and flavor-changing couplings [9,10] come from lattice QCD. It is impractical to cite every development here, but recent reviews [11,12] cover the breadth of progress well.

The results listed above [1–10] have been obtained using staggered fermions [13,14] for the sea quarks, because this approach is numerically the fastest [15]. In the continuum limit, one staggered-fermion field yields four species with a quantum number nowadays called "taste." In numerical lattice gauge theory, sea quarks are represented by a determinant, for staggered fermions,

$$\mathrm{Det}_4(D_{\mathrm{stag}} + m), \tag{1}$$

where D_{stag} denotes the lattice Dirac operator (see below), m is the quark mass, and the subscript 4 is a reminder that the natural outcome is 4 tastes. To simulate a single species of given mass with staggered fermions, the (4-taste) determinant representing the sea is replaced with [16]

$$[\mathrm{Det}_4(D_{\mathrm{stag}} + m)]^{1/4}. \tag{2}$$

Below we shall refer to the systems using (1) and (2) as "unrooted" and "rooted" staggered fermions, respectively. As far as we know, there is no controversy that lattice gauge theory with unrooted staggered fermions (1) defines a four-species continuum gauge theory.

The fourth root is controversial, however, because it is not standard quantum field theory. The arguments supporting its validity hinge on structural properties of unrooted staggered fermions, which suggest that the continuum limit of $\mathrm{Det}_4(D_{\mathrm{stag}} + m)$ in Eq. (2) factors into four equivalent determinants [17–22]. This factorization is verified in weak-coupling perturbation theory, where the $1/4$ from the exponent multiplies each fermion loop. Weak coupling also suggests how the symmetries of four species emerge in the continuum limit. In simplified but similar systems where one can retain analytical control, the rooted determinant is valid [21–23]. Extensive numerical studies elaborate how the procedure works in the Schwinger model [24,25]. Straightforward analysis of the hadron mass spectrum as a function of lattice spacing and quark mass, using chiral perturbation theory, substantiates this picture in detail [11,26]. Further nonperturbative evidence comes from studying the eigenvalues of the staggered-fermion operator D_{stag}, demonstrating that they appear in nearly degenerate quartets [27–30]. On lattice gauge fields with nonzero topological charge, sets of quartets with eigenvalues near zero emerge. The number of quartets and their chirality satisfy the index theorem [29,30].

*g.donald@physics.gla.ac.uk
†c.davies@physics.gla.ac.uk
‡efollana@unizar.es
§ask@fnal.gov

One issue that has not been fully addressed is the behavior of flavor-singlet mesons. Direct calculations of the flavor-singlet meson masses are difficult [31–34], because they entail a contribution in which the quark-antiquark of the meson annihilates into gluons, and the gluons recreate the quark-antiquark pair. With staggered fermions, it is crucial to bear in mind that only the flavor-taste singlet can undergo this process. Low-energy gluons are taste singlets, so a meson with nontrivial taste cannot annihilate into them. The spectrum with two flavors is sketched in Fig. 1, illustrating the roles of the flavor and taste quantum numbers.

Building on the eigenvalue studies, this paper addresses a specific concern, namely that flavor-taste-singlet correlators could diverge as a power of m as $m \to 0$. Such behavior would be a clear failure of rooted staggered fermions. We find fault with key steps in an attempted derivation of this claim [35,36], which uses the 't Hooft vertex [37,38] to try to understand the role of near-zero modes. A complementary examination of the same correlators reduces the problem to certain properties of the near-zero modes' eigenvectors [19]. Then contributions from connected and disconnected correlators cancel the divergent behavior; with the correct combinatoric factors [18,19,39–41], the cancellation holds even with the rooted determinant of Eq. (2).

In this paper, we derive the staggered-fermion 't Hooft vertex directly from the functional integral, both for unrooted and rooted staggered fermions. If unrooted staggered fermions are to obtain a four-species 't Hooft vertex in the continuum limit, we find that the eigenvectors must satisfy the same properties derived in Ref. [19], namely Eqs. (31) and (32) below. References [40,41] tacitly assumed these properties, but we examine the eigenvectors numerically, plotting the quantities that enter the 't Hooft vertex and the flavor-taste-singlet correlators. We find that they behave in precisely the way needed for unrooted and rooted staggered fermions to yield four or, respectively, one species in the continuum limit.

The rest of this paper is organized as follows. Section II discusses staggered fermions and some of the complaints and concerns about Eq. (2). Section III reviews the continuum 't Hooft vertex and its symmetries, constructs the staggered-fermion 't Hooft vertex, and sets up the problem of flavor-taste singlets. This discussion also pinpoints where the analysis of Refs. [35,36] goes astray. Section IV explains details of our numerical setup, gives our lattice results, and discusses their implications. The data speak for themselves: they clearly show that the needed structure emerges dynamically, ever more so for smaller lattice spacing. Section V gives our conclusions. It seems to us that the rooted staggered sea has passed another test in its usual way of relying on properties of the unrooted theory. Appendix A contains some cumbersome notation that lends technical completeness to Secs. II, III, and IV. Appendix B writes out improved actions explicitly. Appendix C remarks on issues of secondary importance, raised in Refs. [35,36].

II. STAGGERED FERMIONS

In this section, we review unrooted staggered fermions, because the way that four species emerge is central to any argument that Eq. (2) is a valid regulator for one species. We are careful to distinguish between flavor and taste; the former is a label decoupled from the gauge interaction; the latter is a property of staggered fermions, described below.

Below we use improved actions to check numerically whether the dynamics of staggered fermions are as expected. For the discussion here, it is enough to start with the original, unimproved lattice action [14]:

$$S_{\text{stag}} = \frac{1}{2}a^3 \sum_{x,\mu} \eta_\mu(x)\bar{\chi}(x)[U_\mu(x)\chi(x+\hat{\mu}a) - U_\mu^\dagger(x-\hat{\mu}a)\chi(x-\hat{\mu}a)] + ma^4 \sum_x \bar{\chi}(x)\chi(x), \quad (3)$$

where a is the lattice spacing, $\chi(x)$ and $\bar{\chi}(x)$ are gauge-group multiplets of Grassmann numbers for lattice site x, $U_\mu(x)$ is a lattice gauge field connecting sites x and $x + \hat{\mu}a$ (such that S_{stag} is gauge invariant), m is the bare mass, $\hat{\mu}$ is a unit vector in the μ direction, and $\mu \in \{1, 2, 3, 4\}$. The staggered-fermion fields carry no Dirac index, and sign factors appear instead of Dirac matrices:

$$\eta_\mu(x) = (-1)^{\sum_{\rho<\mu} x_\rho/a}. \quad (4)$$

The staggered Dirac operator D_{stag} is defined by writing

$$S_{\text{stag}} = a^4 \sum_{x,y} \bar{\chi}(x)(D_{\text{stag}} + m\delta_{xy})\chi(y). \quad (5)$$

The determinant (1) follows from integrating the functional integral over $(\chi, \bar{\chi})$.

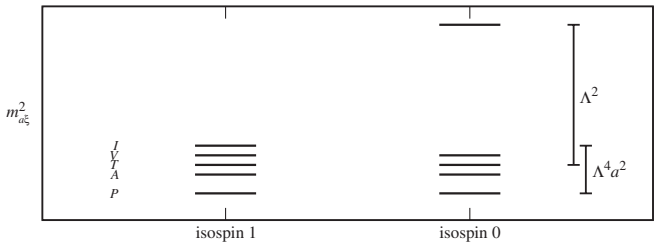

FIG. 1. Pattern of flavor and taste quantum numbers in the (pseudoscalar) meson spectrum with two flavors and four tastes. The flavor-nonsinglet (isospin 1) mesons are split by small lattice artifacts. The flavor-singlet (isospin 0) *taste-nonsinglet* mesons are no different. The flavor-taste singlet, however, receives a contribution from mixing with purely gluonic states, an effect studied in Refs. [31,32].

S_{stag} is invariant under *shifts*:

$$S_\mu: \begin{cases} \chi(x) \mapsto \zeta_\mu(x)\chi(x+\hat{\mu}a) \\ \bar{\chi}(x) \mapsto \zeta_\mu(x)\bar{\chi}(x+\hat{\mu}a) \\ U_\nu(x) \mapsto U_\nu(x+\hat{\mu}a)\ \forall\ \nu, \end{cases} \tag{6}$$

where

$$\zeta_\mu(x) = (-1)^{\sum_{\sigma>\mu} x_\sigma/a}. \tag{7}$$

Acting on fermion fields, $S_\nu S_\mu = -S_\mu S_\nu$. This built-in Clifford group Γ_4 is the origin of the four species in the continuum limit and their quantum number taste. Acting on gauge fields, $S_\nu S_\mu = +S_\mu S_\nu$, from which it follows that low-momentum gauge fields are taste singlets. With n_f flavors of $(\chi, \bar{\chi})$—so $4n_f$ species in all—there is still only one gauge field and, thus, only one Γ_4.

The kinetic term (for n_f flavors) is also invariant under a $\mathrm{U}(n_f)$ symmetry group,

$$\mathrm{U}_\varepsilon: \begin{cases} \chi(x) \mapsto e^{\varphi^a T^a \varepsilon(x)}\chi(x) \\ \bar{\chi}(x) \mapsto \bar{\chi}(x) e^{\varphi^a T^a \varepsilon(x)}, \end{cases} \tag{8}$$

where the T^a are (anti-Hermitian) flavor generators, including flavor-singlet $T^0 = i\mathbb{1}_{n_f}/\sqrt{2n_f}$, and

$$\varepsilon(x) = (-1)^{\sum_{\mu=1}^4 x_\mu/a}. \tag{9}$$

Three crucial properties of these symmetries (8) are that

(1) they are exact even at nonzero lattice spacing a;
(2) they are nonsinglets with respect to taste;
(3) they imply that the eigenvalue spectrum of D_{stag} is pure imaginary and symmetric about 0.

The first property means that these symmetries cannot be anomalous, so they cannot be germane to the index theorem. The second property means that the lack of anomaly is good: in QCD, species-nonsinglet symmetries do not have anomalies. A corollary of the third property ensures that if $i\lambda$ is an eigenvalue of D_{stag} with eigenvector $f(x)$, then $-i\lambda$ is also an eigenvalue, now with eigenvector $\varepsilon(x)f(x)$. This corollary plays an important role in Sec. IV. Unfortunately, the connection between property 3 and the spectrum sometimes leads, it seems, to the flavor-singlet U_ε being misidentified as the analog of continuum QCD's anomalous $\mathrm{U}_A(1)$. The first two properties mean, however, that even the flavor-singlet U_ε cannot be related to $\mathrm{U}_A(1)$.

The analog of the $\mathrm{U}_A(1)$ is a flavor and taste singlet. It is explicitly broken for $a \neq 0$ but restored—apart from the anomaly and mass terms—as $a \to 0$ [14]. This mechanism is familiar in lattice gauge theory [42]; the same happens with Wilson fermions [43]. As $a \to 0$, an anomalous Ward identity emerges with axial-vector current, $A_I^\mu(x)$, and pseudoscalar density, $P_I(x)$, that are taste-flavor singlets [14,44]. The subscript I denotes the trivial representation of the shift symmetries (6), also called the taste-singlet representation.

The way flavor-taste symmetries emerge is crucial to the validity of staggered fermions. In particular,

$$\Gamma_4 \times \mathrm{SU}_V(n_f) \subset \mathrm{SU}_V(4n_f), \tag{10}$$

$$\mathrm{U}_\varepsilon(n_f) \to \mathrm{U}(n_f) \otimes \xi^5 \subset \mathrm{SU}_A(4n_f), \tag{11}$$

where the symmetries on the left are exact (or softly broken) for S_{stag}, and those on the right are desired for continuum QCD. The $\mathrm{SU}_V(n_f)$ on the left-hand side of Eq. (10) is the obvious flavor-number symmetry of Eq. (3) for n_f flavors of equal mass. The ξ^5 on the left-hand side of Eq. (11) denotes the taste-nonsinglet nature of U_ε.

The pattern of symmetry appears most vividly, both for nonzero a and as $a \to 0$, in the meson-mass spectrum. Meson operators can be written $\bar{\chi}\Gamma_\xi\chi$, where Γ_ξ denotes various choices of sign factors η and parallel transport within a hypercube, such that the bilinear transforms under the ξ^{th} bosonic representation of the shift symmetry group Γ_4. As is customary, we label these $\xi \in \{I, V, T, A, P\}$, with V and A each grouping together four of these one-dimensional irreps, and T six. When focusing on a bilinear that transforms under rotations as a scalar, vector, tensor, axial vector, or pseudoscalar, we shall write for Γ_ξ either 1_ξ, γ_ξ^μ, $i\sigma_\xi^{\mu\nu}$, $\gamma_\xi^{\mu 5}$, or γ_ξ^5, as the case may be. For example, in this compact notation the taste-singlet pseudoscalar density is $P_I = \bar{\chi}\gamma_I^5\chi$. Appendix A contains explicit formulas for bilinears in the taste-singlet representation I, for all Γ.

These operators create states such that [45–47]

$$\bar{\chi}\Gamma_\xi T^a \chi \doteq \bar{q}\Gamma\xi T^a q + \mathrm{O}(a^2), \tag{12}$$

where q and $\bar{q}$ are continuum $4n_f$-species fermion fields, on the right-hand side Γ is now a (usual) Dirac matrix, and ξ is now a four-by-four matrix generator of U(4). Together the tensor products $\xi \otimes T$ generate $\mathrm{U}(4n_f)$. For nonsinglet $\xi \otimes T$ the pseudoscalar meson masses depend sensitively on m and a, consistent with chiral perturbation theory [11]. The flavor-taste singlet, with $\xi \otimes T \propto \mathbb{1}_{4n_f}$, should have a mass larger than the rest, cf. Fig. 1, but that has not yet been demonstrated numerically [31]. In this paper, we address this problem by studying the eigenvectors of D_{stag}.

These lines of theoretical and numerical results lead to the picture that [48][1]

$$D_{\text{stag}} + m \doteq (\not{\partial} + m) \otimes \mathbb{1}_4 + a^2\Delta, \tag{13}$$

[1]Reference [48] shows that the U_ε symmetry requires the dimensions-5 terms of the *off-shell* Lee-Sharpe [47] effective Lagrangian to possess coefficients proportional to ma. The apparent $\mathrm{O}(a)$ effects in Refs. [49,50] are an artifact of the choice of field variables.

where $\not{\partial}$ is the continuum Dirac operator, $\mathbb{1}_4$ is the 4×4 unit matrix, $a^2\Delta$ is a taste-symmetry breaking term, and taste-singlet $O(a^2)$ corrections are not written out. Then

$$\mathrm{Det}(D_{\mathrm{stag}} + m) \doteq [\mathrm{Det}_1(\not{\partial} + m)]^4 e^{\mathrm{Tr}_4 \ln a^2\Delta(\not{\partial}+m)^{-1}}, \tag{14}$$

suggesting that

$$[\mathrm{Det}(D_{\mathrm{stag}} + m)]^{1/4} \doteq \mathrm{Det}_1(\not{\partial} + m) \times e^{[\mathrm{Tr}_4 \ln a^2\Delta(\not{\partial}+m)^{-1}]/4}. \tag{15}$$

It is difficult to prove rigorously that the second factor becomes benign as $a \to 0$, although a detailed renormalization-group argument makes it plausible [51,52]. At nonzero a this factor leads to nonlocality [53] (though not the nonlocality discussed in Refs. [54,55]) and violations of unitarity. In this paper, we have nothing to add to the arguments marshalled elsewhere [11,17–20] that these problems go away as $a \to 0$.

A separate line of criticism [35,36] focuses not on the ultraviolet taste breaking of $e^{[\mathrm{Tr}_4 \ln a^2\Delta(\not{\partial}+m)^{-1}]/4}$ but on the interplay of the rooted determinant with correlators built from valence propagators. These papers assert, without derivation, certain symmetries and properties of the 't Hooft vertex that, if true, would imply an unphysical m dependence of multipoint meson correlators. In the next section, we derive, rather than assert, the form of the staggered-fermion 't Hooft vertex. Our derivations pinpoint where Refs. [35,36] go astray. Our derivation further reveals what is needed for staggered fermions to generate the continuum-QCD 't Hooft vertex. Whether staggered fermions behave in the needed way depends on dynamics, for which a numerical test is needed. The (favorable) results of this test are presented in Sec. IV.

III. NEAR-ZERO MODES AND THE 'T HOOFT VERTEX

In this section, we discuss the properties of the near-zero modes in more detail. We review properties of the 't Hooft vertex in continuum gauge theory, with one and with four species. Then we derive the 't Hooft vertex for staggered fermions. We show that the eigenvectors must exhibit a certain structure if unrooted staggered fermions are to tend to the continuum gauge theory. This structure is precisely the criterion presented in Ref. [19] for the rooted theory to have a sensible η' correlator.

A. Continuum QCD

In continuum gauge theories, the Dirac operator can have genuine zero modes. For a single species, the eigenfunctions and eigenvalues are denoted $\not{\partial}\phi_\sigma = i\lambda_\sigma\phi_\sigma$, where λ is real, and integer σ labels the modes. For the modes with nonzero eigenvalue, it is convenient to take $\sigma > 0$ ($\sigma < 0$) for modes with $\lambda > 0$ ($\lambda < 0$). These modes come in conjugate pairs: $\lambda_{-\sigma} = -\lambda_\sigma$, $\phi_{-\sigma} = \gamma^5\phi_\sigma$. In the subspace of zero modes, $\lambda = 0$, the eigenfunctions can be chosen such that $\gamma^5\phi_\iota^{(\pm)} = \pm\phi_\iota^{(\pm)}$, with the integer label ι ranging from 1 to $k_\pm$. For n species, the Dirac operator is $\not{\partial}\mathbb{1}_n$, with eigenfunctions $\phi_\sigma e^{(\tau)}$, where the $e^{(\tau)}$ form an orthonormal basis in species space. The number and chirality of zero modes is related to the topological charge Q via the index theorem [56,57]

$$n_+ - n_- = nQ, \tag{16}$$

where n is the number of species, and $n_\pm = nk_\pm$ accounts for the species multiplicity.

The determinant acquires a factor of mass m from each zero mode. As $m \to 0$ it would seem that such gauge fields would drop out of the ensemble average. But if one looks at the eigenvalue-eigenfunction representation of the propagator, one finds powers of $1/m$ that cancel the powers of m from the determinant. Focusing on $|Q| = 1$ and $n = 1$, so that there is one zero mode, the propagator is ($\langle\bullet\rangle_{|Q|=1}$ denotes average over $|Q| = 1$ gauge fields)

$$\begin{aligned}\langle\psi(x)\bar{\psi}(y)\rangle &= \left\langle m\prod_{\sigma>0}(\lambda_\sigma^2 + m^2)\sum_\sigma \frac{\phi_\sigma(x)\phi_\sigma^\dagger(y)}{i\lambda_\sigma + m}\right\rangle_A \\ &= \left\langle\prod_{\sigma>0}(\lambda_\sigma^2 + m^2)\phi_0(x)\phi_0^\dagger(y)\right\rangle_{|Q|=1} + O(m),\end{aligned} \tag{17}$$

where ϕ_0 is now used for the zero-mode eigenfunction. One sees that the mode with $\lambda = 0$ has a canceling factor of $1/m$. The factor $\phi_0(x)\phi_0^\dagger(y)$ is the 't Hooft vertex [37,38]. (If ϕ_0 is localized, as it is around instantons, then the "vertex" has support only for x, y near the center of localization.) For the four-point function, there are superficially two powers of $1/m$, but two contributions identical apart from their opposite sign cancel each other. This is simply the Pauli exclusion principle arising from the Grassmann nature of the fields.

With $n = 4$ fermion species, each mode is replicated four times, so gauge fields with $|Q| = 1$ yield four zero modes, one per species. The determinant yields a factor m^4, which is not compensated until the eight-point function:

$$\begin{aligned}&\left\langle\prod_{f=1}^4 \psi_f(x_f)\bar{\psi}_f(y_f)\right\rangle \\ &= \left\langle\prod_{\sigma>0}(\lambda_\sigma^2 + m^2)^4\prod_{f=1}^4\phi_0(x_f)\phi_0^\dagger(y_f)\right\rangle_{|Q|=1} + O(m),\end{aligned} \tag{18}$$

with four factors like that in Eq. (17). In higher-point functions, Pauli exclusion again ensures that contributions singular in m cancel. Below we are interested in flavor-singlet meson correlators, such as (flavor index contracted; $n_f = 4$)

$$\left\langle \prod_{f=1}^{4} \bar{\psi}\Gamma_f \psi(x_f) \right\rangle = 24 \left\langle \prod_{\sigma>0} (\lambda_\sigma^2 + m^2)^4 \prod_{f=1}^{4} \phi_0^\dagger \Gamma_f \phi_0(x_f) \right\rangle_{|Q|=1} + \mathrm{O}(m), \quad (19)$$

where the combinatoric factor 24 obtains after cancellations between many (dis)connected terms.

Let us now examine a property of the 't Hooft vertex that is central to Creutz's arguments [35,36]. Under the anomalous $\mathrm{U}_A(1)$ transformation

$$\psi \mapsto e^{i\gamma^5\alpha/2}\psi, \qquad \bar{\psi} \mapsto \bar{\psi} e^{i\gamma^5\alpha/2}, \quad (20)$$

the n-species 't Hooft vertex transforms as

$$\prod_{f=1}^{n} \phi_0(x_f)\phi_0^\dagger(y_f) \mapsto e^{\pm in\alpha} \prod_{f=1}^{n} \phi_0(x_f)\phi_0^\dagger(y_f), \quad (21)$$

where the sign is the chirality of the zero mode, $\gamma^5\phi_0 = \pm\phi_0$. If α is a multiple of $2\pi/n$, the prefactor is unity; thus, the 't Hooft vertex remains invariant under a $\mathbb{Z}_n$ subgroup of $\mathrm{U}_A(1)$ [58].

This invariance holds for the full determinant [59,60]. Under the transformation (20) with $\alpha = 2\pi/n$, one has

$$m^{n(n_+ + n_-)} e^{i(n_+ - n_-)2\pi/n} \mathrm{Det}'_n[\not{\partial} + m e^{i\gamma^5 2\pi/n}] = m^{n(n_+ + n_-)} \mathrm{Det}'_n[\not{\partial} + m e^{i\gamma^5 2\pi/n}], \quad (22)$$

where Det'_n denotes the n-species determinant with zero modes projected out. The right-hand side follows because, by Eq. (16), the phase on the left-hand side is trivial. Because $e^{i2\pi/n} = e^{-i2\pi(n-1)/n}$, the twisted mass $m e^{i\gamma^5 2\pi/n}$ can be removed with nonsinglet $\mathrm{SU}_A(n)$ transformations, namely,

$$\psi \mapsto e^{-i\gamma^5 \Xi\pi/n}\psi, \qquad \bar{\psi} \mapsto \bar{\psi} e^{-i\gamma^5 \Xi\pi/n}, \quad (23)$$

where $\Xi = \mathrm{diag}(1, \ldots 1, -(n-1))$, or any permutation thereof. The composition of transformations (23) and (20) with $\alpha = 2\pi/n$ returns the original determinant, $m^{n(n_+ + n_-)}\mathrm{Det}'_n(\not{\partial} + m)$. We have shown here that the $\mathbb{Z}_n$ in question is not only a subset of the anomalous $\mathrm{U}_A(1)$, but also the center of the exact $\mathrm{SU}_A(n)$. In fact, $\mathbb{Z}_n$ is the intersection of the $\mathrm{SU}_A(n)$ and $\mathrm{U}_A(1)$.

B. Unrooted staggered fermions

Now we would like to see how staggered fermions reproduce the four-species 't Hooft vertex. Let us now denote the eigenvectors and eigenvalues $D_{\mathrm{stag}} f_s(x) = i\lambda_s f_s(x)$. We use f for the eigenvectors of D_{stag}, instead of ϕ for the eigenfunctions of $\not{\partial}$, because our aim is to study whether and how a structure like $\phi_\sigma e^{(\tau)}$ arises from the f_s. As before, it is convenient to choose $s > 0$ ($s < 0$) for $\lambda_s > 0$ ($\lambda_s < 0$). As mentioned above, the function $f_{-s}(x) = \varepsilon(x) f_s(x)$ has eigenvalue $\lambda_{-s} = -\lambda_s$, which follows from the U_ε symmetry. One must bear in mind that the relation between eigenvectors $f_{\pm s}$ originates from a different flavor of symmetry than the relation between eigenfunctions $\phi_{\pm\sigma}$. In the notation introduced above Eq. (12), multiplication by $\varepsilon(x)$ corresponds to γ_P^5, a taste nonsinglet that, in a continuum four-species theory, looks like $\gamma^5\xi^5$, not $\gamma^5\mathbb{1}_4$.

The first step is to single out the modes analogous to the zero modes in the continuum theory. With staggered (and most other lattice) fermions, no exact zero modes arise, but one expects D_{stag} to have some exceptionally small eigenvalues [44]. A crisp way to identify them is via the spectral flow of the operator [61]

$$H_{\mathrm{stag}} = -iD_{\mathrm{stag}} + \mu\gamma_I^5, \quad (24)$$

with $H_{\mathrm{stag}} f_s(x;\mu) = \lambda_s(\mu) f_s(x;\mu)$; the eigenvalues of D_{stag} are $i\lambda_s(0)$. From the U_ε symmetry, $f_{-s}(x;\mu) = \varepsilon(x) f_s(x;-\mu)$, $\lambda_{-s}(\mu) = -\lambda_s(-\mu)$. Near-zero modes are those with a nearby zero crossing, $\lambda(\mu_0) = 0$ for $\mu_0 \ll \Lambda$. The (taste-singlet) chirality is then

$$\hat{\mathcal{X}}_s = \mathrm{sign}\lambda'_s(\mu_0), \quad (25)$$

where the prime denotes differentiation with respect to μ. Taking the U_ε symmetry into account, we can label the positive-chirality modes $f_i^{(+)}$ with $i > 0$ ranging from $1, \ldots, \ell_+$ (λ_i slightly positive) and $i < 0$ ranging from $-1, \ldots, -\ell_+$ (λ_i slightly negative). A similar labeling scheme can be adopted for the $2\ell_-$ negative-chirality modes $f_i^{(-)}$. Note that [61]

$$\lambda'_s(\mu_0) \approx \lambda'_s(0) = \sum_x f_s^\dagger(x)\gamma_I^5 f_s(x) \equiv \mathcal{X}_s, \quad (26)$$

where $\mathcal{X}_s$ is a more common way to identify chirality [62]. Modes s and $-s$ have the same value of taste-singlet chirality (whether defined by $\mathcal{X}_s$ or $\hat{\mathcal{X}}_s$), because γ_I^5 implies transport over an even number of links and, consequently, the ε sign factors at the two ends of γ_I^5 are the same.

The spectral flow is elegant but computationally demanding. It is also possible to identify the near-zero modes by looking for modes with λ sufficiently small and $\mathcal{X}$ sufficiently close to ± 1. Although the spectral flow is (presumably) more decisive in borderline cases, in practice, especially for the scope of this paper, the computational demand seems prohibitive. In Sec. IV, we shall therefore rely on our experience in Refs. [27,30] of using $(\lambda, \mathcal{X})$ to identify the near-zero modes.

If staggered fermions generate four species in the continuum limit, then the eigenvalues should arrange themselves into closely spaced quartets. For nonzero modes, four modes should cluster around some distinctly nonzero value. For near-zero modes, on the other hand, such quartets lie slightly above and below the real axis. U_ε symmetry dictates that a mode and its ε partner have

the same chirality and, thus, may be assigned to the same quartet. If the gauge-field dynamics yield even $\ell_\pm = 2k_\pm$, then one has quartets. The resulting index theorem is then ($n_\pm = 4k_\pm$)

$$n_+ - n_- = 4Q, \tag{27}$$

where Q is a pure-gauge definition of topological charge. For smooth enough fields and for extensions of Eq. (3) that smooth out the interaction, both kinds of quartets emerge [27,28], as does the connection between gauge-field topology and the index [27–30].

With one fermion field but sets of four near-zero modes, the combinatorics underlying the 't Hooft mechanism are less straightforward than in four-species continuum theories. Let us focus on $|Q| = 1$. Two pairs of near-zero modes appear with eigenvalues $\pm i\lambda_i$, $i = 1, 2$. "Small" means $|\lambda_i| \sim (a\Lambda)^{p_\lambda}\Lambda$; a power law with $p_\lambda = 1$ or 2 suffices, and one expects $p_\lambda = 2$ [48]. Moreover, $\mathcal{X}_1$ and $\mathcal{X}_2$ have the same sign (with several actions [27,30]), and we shall see in Sec. IV that these features also hold for the highly improved staggered-quark (HISQ) action [63].

To derive the 't Hooft vertex explicitly, let us examine the (fermion) eight-point function, which for staggered fermions is

$$\left\langle \prod_{f=1}^{4} \chi(x_f)\bar{\chi}(y_f) \right\rangle = \left\langle \prod_{i=1}^{2}(\lambda_i^2 + m^2) \prod_{s>0}(\lambda_s^2 + m^2) \det_{(f,g)} G(x_f, y_g) \right\rangle_{|Q|=1}, \tag{28}$$

where the propagator

$$G(x, y) = \langle \chi(x)\bar{\chi}(y)\rangle_{\chi,\bar{\chi}} = \sum_{\text{all } s} \frac{f_s(x) f_s^\dagger(y)}{i\lambda_s + m} \tag{29}$$

with the sum running over near-zero and nonzero modes. Neglecting in Eq. (28) the near-zero λ_i relative to m, the near-zero-mode terms contribute to Eq. (28) as

$$m^4 \det_{(f,g)} G(x_f, y_g) = \det_{(i,f)} f_i(x_f) \det_{(j,g)} f_j^\dagger(y_g) + \mathrm{O}(m), \tag{30}$$

where $i, j \in \{-2, -1, 1, 2\}$. In higher-point functions, the Pauli exclusion again ensures that contributions singular in m cancel.

The product of determinants on the right-hand side of Eq. (30) is the 't Hooft vertex for (unrooted) staggered fermions. To reproduce the product of four factors of $\phi_0\phi_0^\dagger$ in Eq. (18), the four staggered eigenfunctions f_i, $i \in \{-2, -1, 1, 2\}$, must have structure similar to $\phi_0(x)e^{(i)}$. One could seek such structure in a basis where a taste index looks obvious, but because taste is, fundamentally, a quantum number of the shifts, i.e., single-link translations, gauge-dependent roughness of the gauge field would obscure it.

The way forward is to contract the χ and $\bar{\chi}$ fields into color singlets. The contractions must also be taste singlets, because a nonsinglet corresponds to $e^{(i)\dagger}\xi e^{(j)}$, $\xi \neq \mathbb{1}_4$, which need not vanish when $j \neq i$. In Eq. (28) we thus replace $\chi(x_f)\bar{\chi}(y_f)$ with a taste singlet $\bar{\chi}\Gamma_I^f\chi(x_f)$. Contracting Eq. (30) in this way, one is led to consider

$$\zeta_{ij}^\Gamma(x) = f_i^\dagger \Gamma_I f_j(x) \tag{31}$$

with, recall, some parallel transport implied by Γ_I. The 't Hooft vertex simplifies in the desired way if

$$\zeta_{ij}^\Gamma(x) \propto \delta_{ij}[1 + \mathrm{O}(a^{p_{\zeta^\Gamma}})], \tag{32}$$

for $\Gamma_I = 1_I, \gamma_I^5, i\sigma_I^{\mu\nu}$. If, further, the proportionality fulfilled by an (approximately) i-independent diagonal $\zeta_{ii}^\Gamma(x)$, ζ_{ij}^Γ would then mimic $\phi_0^\dagger\Gamma\phi_0 e^{(i)\dagger}e^{(j)} \propto \delta_{ij}$. Approaching this limit as a power law with $p_{\zeta^\Gamma} = 1$ or 2 suffices, and one expects $p_{\zeta^\Gamma} = 2$ [48]. Section IV presents numerical results for these local overlaps, including a dependence.

For $\Gamma_I = \gamma_I^\mu, \gamma_I^{\mu 5}$, the local overlaps ζ_{ij}^Γ behave somewhat differently. In continuum gauge theory, the zero modes satisfy $\phi_\iota^{(\pm)\dagger}\gamma^\mu\phi_\iota^{(\pm)} = \phi_\iota^{(\pm)\dagger}\gamma^{\mu 5}\phi_\iota^{(\pm)} = 0$, because γ^5 anticommutes with γ^μ and $\gamma^5\phi_\iota^{(\pm)} = \pm\phi_\iota^{(\pm)}$. The spin and taste degrees of freedom emerge from staggered fermions via the same dynamical mechanism, so the diagonal $\zeta_{ii}^{\gamma^\mu}$ and $\zeta_{ii}^{\gamma^{\mu 5}}$ should vanish commensurately with the off-diagonal ζ_{ij}^Γ, $\Gamma_I = 1_I, \gamma_I^5, i\sigma_I^{\mu\nu}$.

The local overlaps of continuum nonzero modes of different species also vanish (trivially, because $e^{(\tau_1)\dagger}e^{(\tau_2)} = \delta_{\tau_1\tau_2}$). Therefore, within a quartet of staggered-fermion nonzero modes, continuum QCD is reproduced if ζ_{rs}^Γ, $r \neq s$, also vanish as $a \to 0$.

Assuming Eq. (32) holds, it is easy to see that

$$\left\langle \prod_{f=1}^{4} \bar{\chi}\Gamma_{If}\chi(x_f) \right\rangle = \left\langle \prod_{\sigma>0}(\lambda_\sigma^2 + m^2)^4 \sum_{(ijkl)} \zeta_{ii}^{\Gamma_1}(x_1)\zeta_{jj}^{\Gamma_2}(x_2)\zeta_{kk}^{\Gamma_3}(x_3)\zeta_{ll}^{\Gamma_4}(x_4) \right\rangle_{|Q|=1} + \mathrm{O}(m), \tag{33}$$

where the sum runs over the $4! = 24$ ways of choosing distinct $(ijkl)$ from $\{-2, -1, 1, 2\}$.

Let us now discuss the $\mathbb{Z}_n$ (now $\mathbb{Z}_{4n_f}$) symmetry mentioned at the end of Sec. III A. The anomalous $\mathrm{U}_A(1)$ and most of the softly broken, nonanomalous $\mathrm{SU}_A(4n_f)$ emerge only in the continuum limit. Some passages in Refs. [35,36] seem to assign a pertinent role to the $\mathrm{U}_\varepsilon(n_f)$ symmetries, which are exact even at nonzero a. These symmetries are a distraction at best: the group $\mathrm{U}_\varepsilon(n_f)$ intersects with the relevant $\mathbb{Z}_{4n_f}$, which is the center of $\mathrm{SU}(4n_f)$, only at $-\mathbb{1}_{4n_f}$.

C. Rooted staggered sea

With rooted staggered fermions, two changes are carried out. In addition to using the rooted determinant (2), the simple combinatorics of $\det_{(f,g)} G(x_f, y_g)$ must also change [39]. For example, the taste-singlet pseudoscalar meson propagator is replaced with

$$\langle \bar{\chi}\gamma_I^5\chi(x)\bar{\chi}\gamma_I^5\chi(y)\rangle_U \to -\frac{1}{4}C(x,y) + \frac{1}{16}D(x,y), \quad (34)$$

where the connected and disconnected contributions are

$$C(x,y) = \langle \mathbb{D}\,\mathrm{tr}[\gamma_I^5 G(x,y)\gamma_I^5 G(y,x)]\rangle_U, \quad (35)$$

$$D(x,y) = \langle \mathbb{D}\,\mathrm{tr}[\gamma_I^5 G(x,x)]\mathrm{tr}[\gamma_I^5 G(y,y)]\rangle_U, \quad (36)$$

where $\mathbb{D}$ is the rooted determinant (2), the trace is over color, and the translations implied by γ_I^5 act to the right (left) on the first (second) argument of G. The correlator in Eq. (34) couples to the analog of the flavor-singlet η' meson in QCD, and similar constructions hold for other taste-singlet bilinears.

The combinatoric factors in Eq. (34) follow immediately from considering [18,19,40,41]

$$\{\mathrm{Det}_{n_f}[(\not{\partial} + m)\otimes \mathbb{1}_4]\}^{n/4}, \quad (37)$$

where—inside the braces—one has four copies of n_f noncontroversial fermions. Equation (37) together with a source for a single species provide an engine to generate the combinatorics of rooting (in general): to obtain n species from 4, a term with t traces over color receives a factor [39]

$$\left(-\frac{n}{4}\right)^t. \quad (38)$$

For Eq. (37) to be relevant to staggered fermions, the dynamics must ensure Eq. (13) and, in particular, Eq. (32), as we now show. The single-flavor determinant becomes (for $|Q| = 1$)

$$\prod_{i=1}^{2}(\lambda_i^2 + m^2)^{1/4}\prod_{s>0}(\lambda_s^2 + m^2)^{1/4}. \quad (39)$$

Neglecting λ_i compared to m again, the first product collapses to $|m|$. The near-zero-mode contributions are then

$$C(x,y) = \sum_{i,j}\left\langle \frac{|m|\mathbb{D}'}{m^2}\zeta_{ij}^{\gamma^5}(x)\zeta_{ji}^{\gamma^5}(y)\right\rangle_{|Q|=1}, \quad (40)$$

$$D(x,y) = \sum_{i,j}\left\langle \frac{|m|\mathbb{D}'}{m^2}\zeta_{ii}^{\gamma^5}(x)\zeta_{jj}^{\gamma^5}(y)\right\rangle_{|Q|=1}, \quad (41)$$

where $\mathbb{D}'$ is the $s>0$ product in Eq. (39), and $i,j \in \{-2,-1,1,2\}$. If Eq. (32) holds, then the sum in Eq. (40) collapses to terms with $i = j$, apart from lattice artifacts. Thus, C has four contributions singular in $1/|m|$, whereas D has 16. With the correct combinatoric factors, they cancel.

It is, perhaps, instructive to exhibit the three-point correlator. Assuming Eq. (32) and homing in on the zero-mode contributions,

$$\begin{aligned}\bar{\chi}\Gamma_{I1}\chi(x_1)\bar{\chi}\Gamma_{I2}\chi(x_2)\bar{\chi}\Gamma_{I3}\chi(x_3) \to &-\frac{1}{4}\{\mathrm{tr}[\Gamma_{I1}G(x_1,x_2)\Gamma_{I2}G(x_2,x_3)\Gamma_{I3}G(x_3,x_1)] + 1\ \text{perm}\}\\ &+\frac{1}{4^2}\{\mathrm{tr}[\Gamma_{I1}G(x_1,x_1)]\mathrm{tr}[\Gamma_{I2}G(x_2,x_3)\Gamma_{I3}G(x_3,x_2)] + 2\ \text{perms}\}\\ &-\frac{1}{4^3}\,\mathrm{tr}[\Gamma_{I1}G(x_1,x_1)]\mathrm{tr}[\Gamma_{I2}G(x_2,x_2)\mathrm{tr}[\Gamma_{I3}G(x_3,x_3)] \quad (42)\end{aligned}$$

$$\to \frac{|m|}{m^3}(-2+3-1)\zeta^{\Gamma_1}(x_1)\zeta^{\Gamma_2}(x_2)\zeta^{\Gamma_3}(x_3)\zeta^{\Gamma_4}(x_4), \quad (43)$$

where $|m|$ comes from the rooted determinant. Here sums over the four staggered-fermion near-zero modes cancel the explicit factors of $\frac{1}{4}$. The $|m|/m^2$ contributions cancel in a similar way. Earlier work [18,40,41], tacitly assumed Eq. (32); in particular, Ref. [41] shows how the combinatorics work for higher-point 't Hooft-vertex effects.

In Refs. [35,36,64], Creutz disregards the cancellations stemming from the correct weighting of different contributions to flavor-taste-singlet correlators. He considers more primitive combinations, like any individual line in Eq. (42), which clearly are singular as $m \to 0$. He then draws two incorrect inferences. First, he claims that the normal cancellations connected with Pauli statistics cannot arise. Combining the correct weights with the assumption (tested below) Eq. (32), one sees that this is not the case. The outcome is not too mysterious: as taste emerges into a species-like quantum number, the correct set of correlators averages over them.

The other misstep is to assert that the $\mathbb{Z}_{4n_f}$ symmetry of the unrooted 't Hooft vertex cannot be reduced to $\mathbb{Z}_{n_f}$. This

is incorrect, because, while the rooted determinant clearly retains the symmetries of the unrooted determinant, the 't Hooft vertex stems from the combined behavior of determinant and valence propagators. The replacement of the combinatoric factors of traces with (38) effectively projects the symmetry emerging in the chiral limit from SU($4n_f$) [taking $n = 1$ in (38)] to SU(n_f). Since the relevant symmetry is the center of the emergent flavor symmetry, one has $\mathbb{Z}_{n_f}$.

Many of these points have been made before [18,40,41,65], but until now it has always been assumed that the tastes decouple as posited in Eq. (32). (Reference [19] noted the necessity of this assumption.) Our approach can easily be extended to taste-nonsinglet flavor-singlet correlators, and the properties of the local overlaps with nonsinglet Γs will not enjoy the cancellation. We shall now compute the ζ_{ij}^{Γ} nonperturbatively, to find out whether the tastes couple to each other at the strong scale Λ_{QCD} or at the cutoff scale a^{-1}.

IV. NUMERICAL RESULTS

In this section we present our numerical methods and results. First we explain the motivation for studying improved discretizations and why it suffices to compute their eigenvalue spectrum on quenched gauge fields. We present results for eigenvalues and chirality with the HISQ action. These results are qualitatively similar to those obtained with the Asqtad and Fat7 $\times$ Asqtad actions in Refs. [27,30], so we focus here on $|Q| = 1$. Then we show results for the overlaps, ζ_{ij}^{Γ}, defined in Eq. (31), and test their behavior as a function of lattice spacing against Eq. (32). Finally we discuss correlators for mesons of different J^P in turn, starting with pseudoscalars where the issues are particularly important. Taken together, our results demonstrate how the behavior of the different contributions from near-zero and nonzero modes matches that expected in the continuum.

A. Methods

In this paper, we use the same ensembles of SU(3) gauge fields as in earlier studies of eigenvalues and chirality [27,30]. They are quenched configurations, omitting the effects of sea quarks. They are generated with a Symanzik-improved gauge action, so that the tree-level a^2 errors are removed [66], and tadpole-improved couplings in this action, so that loop corrections are reduced [67]. Three different values of the gauge coupling are used, giving three widely separated values of the lattice spacing, covering the range of typical unquenched lattice-QCD calculations [11], so our results should pertain directly to them. At the middle value of the three lattice spacings, we have three different-sized lattices in order to check the volume dependence. The parameters for the configurations are given in Table I.

TABLE I. Details of the gauge configurations used: β is the bare gauge coupling, a the lattice spacing [68], V the spacetime volume in lattice units, and L the linear size in physical units. The final column gives the number of configurations in each ensemble with $|Q| = 1$. We refer to set 1 as having a "coarse" lattice spacing, sets 2, 3, and 4 as "intermediate", and set 5 as "fine."

Ensemble	β	a (fm)	V	L (fm)	#{$\lvert Q\rvert = 1$}
1	4.6	0.125	12^4	1.50	294
2	4.8	0.093	12^4	1.12	806
3	4.8	0.093	16^4	1.49	424
4	4.8	0.093	20^4	1.86	288
5	5.0	0.077	20^4	1.54	430

It is sufficient to study these issues in the quenched approximation, because we aim to test a structural property of staggered fermions in fixed-Q sectors. In particular, omitting the determinant decouples Creutz's infrared concerns from others' ultraviolet concern that taste breaking remains in the continuum limit. If the eigenvectors satisfy Eq. (32) strongly enough, then the 't Hooft vertex and the consequent cancellation of mass-singular contributions to the connected and disconnected flavor-singlet meson correlators should work out in general. We shall see that this is the case.

With the original staggered-fermion action, Eq. (3), the interaction connects adjacent sites. Very large discretization errors arise in a wide range of observables, washing out the expected quartet structure in the eigenvalue spectrum. These discretization errors have been traced to taste-changing interactions from gluons with one or more components of momentum $p_\mu \approx \pi/a$ [69]. Because of the gluon exchange, these effects are formally of order $\alpha_s a^2$, i.e., α_s times smaller than normal discretization effects [70]. In order to reduce these taste-changing effects, it is necessary to smear the gauge field, replacing U_μ and $U_\mu^\dagger$ in Eq. (3) with sums of products of link matrices tracing out more complicated paths between x and $x \pm \hat{\mu} a$ [69,71,72].

Several staggered-fermion actions have been developed along these lines. The Asqtad [73] and Fat7 $\times$ Asqtad [30] actions exhibit a reduction, relative to the nearest-neighbor action in Eq. (3), in splittings between pseudoscalar mesons of different taste [26,30]. Similarly, with these actions the quartet structure of the eigenvalue spectrum more clearly emerges [27,30].

Here we have calculated low-lying eigenvalues and eigenvectors for the highly improved staggered-quark (HISQ) action [63], reusing the same gauge-field configurations. The HISQ action supersedes the Fat7 $\times$ Asqtad action; it is essentially the same but corrects the smearing at the second stage to remove fully the discretization errors that the smearing introduces. As we shall see in Sec. IV B this change makes only a small effect. The eigenvalue

quartet structure is very clear with the HISQ action, which is reflected in other properties that, by now, have been thoroughly tested: small pseudoscalar mass splittings and small discretization errors, even for heavy quarks [9,63,74,75].

Appendix B provides explicit equations for the smeared actions.

We use the Lanczos algorithm to calculate the low-lying eigenvalues, $i\lambda$, of the anti-Hermitian massless HISQ Dirac operator, D_{HISQ}, defined implicitly in Eq. (B6). Owing to its red-black checkerboard structure, the calculations can be simplified by using the Hermitian positive semidefinite operator $-D^2_{\mathrm{HISQ}}$, projected onto either the red (even) or black (odd) sites of the lattice. This yields λ^2, from the smallest values upwards, and eigenvector f, on the chosen half of the lattice. The eigenvalues of D_{HISQ} are then $\pm i\lambda$, and the corresponding eigenvector on the other half of the lattice is $\pm D_{\mathrm{HISQ}} f/i\lambda$. This construction automatically implements the requirement that the eigenvectors corresponding to eigenvalues $i\lambda$ and $-i\lambda$ are simply related by multiplication with $\varepsilon(x)$. Thus, on the odd (even) sites, the $-s$th eigenvector is opposite (same) in sign as the $+s$th eigenvector.

B. Eigenvalues and chirality with HISQ

Figure 2 shows the four near-zero eigenvalues as well as the 16 pairs of nonzero eigenvalues of D_{HISQ} with smallest $|\lambda|$, obtained on typical $|Q| = 1$ configurations from ensembles labeled 1 (coarse), 3 (intermediate), and 5 (fine) in Table I. These lattices have similar physical volume but lattice spacing varying from 0.125 to 0.077 fm. The anticipated picture is unmistakable: four (and only four) very small eigenvalues appear, followed by distinct quartets. As the lattice spacing decreases, eigenvalues within a quartet come closer and closer to being degenerate, typically by forming two close-by almost degenerate pairs. The near-zero modes are typically, on these lattices, at least an order of magnitude smaller than the low-lying nonzero modes.

The Lanczos algorithm also gives the eigenvectors corresponding to these eigenvalues. Normalizing them to have modulus 1, we compute the chirality χ in Eq. (26), using the smeared W_μ matrices [Eq. (B5)] instead of U_μ. Reference [30] showed that it makes little qualitative difference to the results whether the original U_μ, Asqtad V_μ [Eq. (B2)], or Fat7 $\times$ Asqtad $\check{W}_\mu$ [Eq. (B8)] are used. The numerical values of the chirality may change, but the picture remains qualitatively the same.

Because lattice artifacts break the taste-singlet symmetry, the chirality defined in Eq. (26) takes values that are not simply 1 and 0 [62]. References [27,30] found, however, that it is easy, especially with improved gauge and staggered-fermion actions, to separate the near-zero modes with relatively large chirality, close to 1, from the other modes with chirality close to 0. The number of near-zero modes defined this way agrees with the index theorem, Eq. (27), and pure-gauge definitions of the topological charge. The agreement between the index and the gauge-field topological charge improves as the lattice spacing gets smaller. On the $a = 0.077$ fm ensemble, the disagreement for Asqtad and Fat7 $\times$ Asqtad is just 2% [30], which is no worse than the ambiguity between different gluonic definitions. For this paper, we therefore simply take the index to classify the topology.

Figure 3 shows the chirality values for the HISQ action versus eigenvalues on all configurations defined to be of

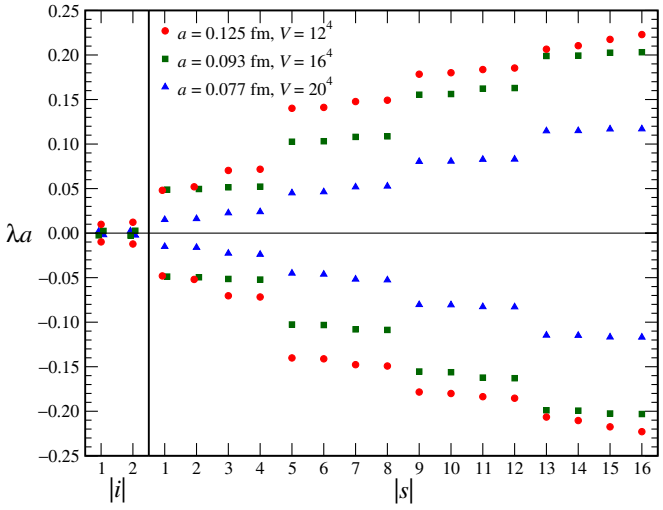

FIG. 2 (color online). The four near-zero eigenvalues (left panel) and the 16 lowest-lying nonzero pairs of D_{HISQ} eigenvalues on a typical $|Q| = 1$ configuration from sets 1 (red circles), 3 (green squares), and 5 (blue triangles). For clarity, some modes are offset horizontally.

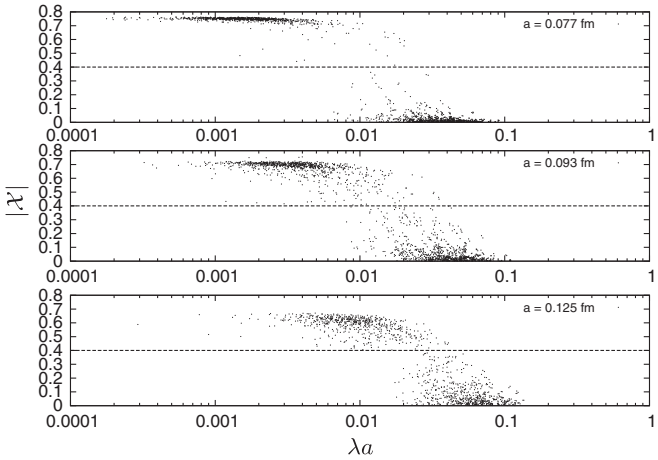

FIG. 3. The absolute value of the chirality $|\chi|$ plotted against eigenvalue, λa, in lattice units for the four lowest (positive) eigenvalues for the $|Q| = 1$ configurations in ensembles 1, 3, and 5. The dotted line on each graph indicates $|\chi| = 0.4$, which is used to separate large and small chirality in determining the value of Q (see text).

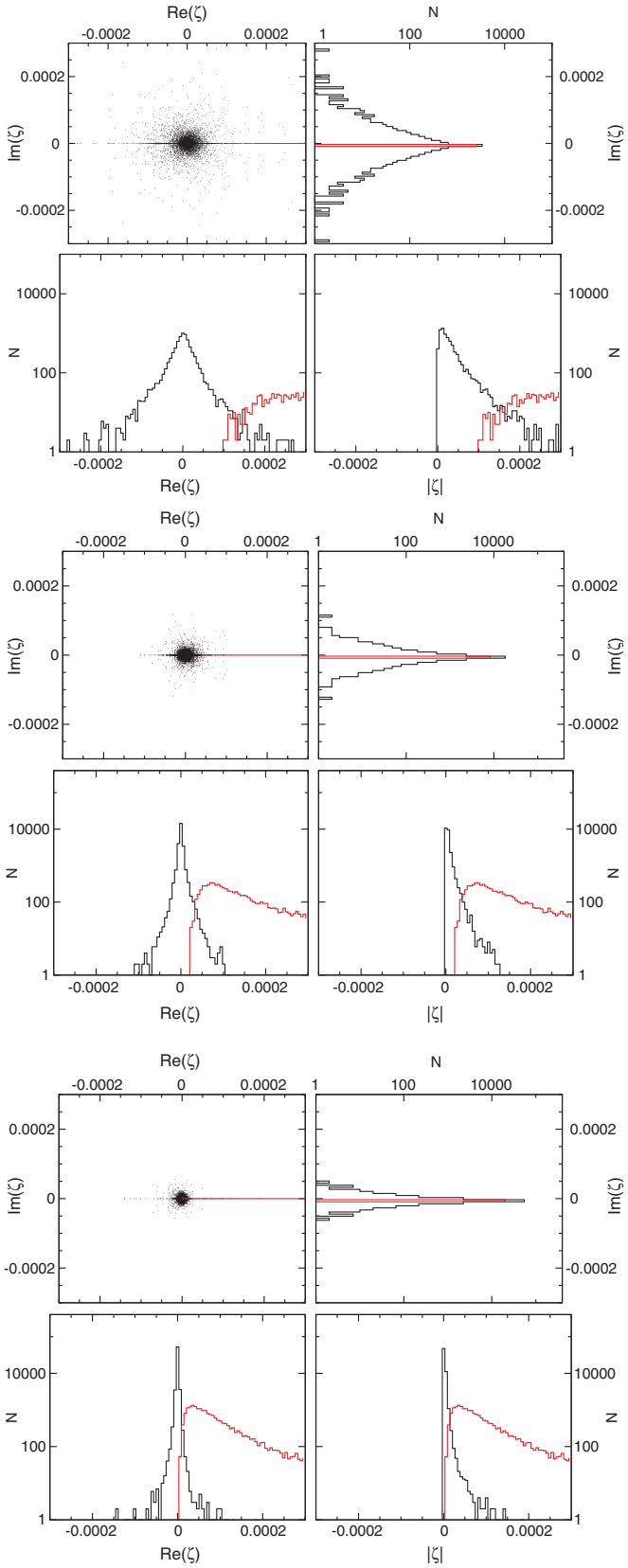

FIG. 4 (color). ζ^1_{ij} on coarse (top), intermediate (middle), and fine (bottom) $|Q| = 1$ gluon field configurations, with $j = i$ (red) and $j \neq i$ (black), $i, j = \pm 1, \pm 2$. Note the logarithmic y-axis scale for the histograms.

topological charge ± 1 via the index. To reduce clutter, Fig. 3 shows only the two near-zero modes and the two lowest-lying nonzero modes. (Because $\mathcal{X}_{-s} = \mathcal{X}_s$, we count only the positive-λ modes here.) One sees a clear separation of large and small chirality values, especially so on the finer configurations. Although the values corresponding to the maximum chirality do not change very markedly from coarse to finer lattices, the spread of results becomes much narrower. The small chirality values, corresponding to nonzero eigenmodes, fall rapidly to zero with lattice spacing. We take $\mathcal{X} > 0.4$ (drawn on the graphs) to indicate large chirality and then count the number of eigenvalues (with positive λ) that have large chirality. Configurations with two (positive-λ) large-chirality modes are taken to be $|Q| = 1$ configurations. Table I lists the number of such configurations for each ensemble. More general scatter plots with results at $|Q| > 1$ and the Asqtad and Fat7 $\times$ Asqtad actions have been given in Ref. [30], and with HISQ look very similar.

C. Results for ζ^Γ_{ij}

Using the eigenvectors determined in the previous section we now go on to look in more detail at the overlaps of the near-zero-mode eigenvectors that are relevant to the 't Hooft vertex. Figures 4–6 show scatter plots and histograms of the ζ^Γ_{ij} distributions for $\Gamma = 1$, γ^5, and γ^μ, and $i, j = \pm 1, \pm 2$ on one or two configurations, ranging over all x. Each figure displays this information, from top to bottom, for the coarse ($a = 0.125$ fm), intermediate ($a = 0.093$ fm), and fine ($a = 0.077$ fm) lattices, at (nearly) fixed physical volume (sets 1, 3, and 5). The four panels in each case show the scatter of ζ^Γ_{ij} in the complex plane (upper left), the histogram for $\mathrm{Re}\zeta^\Gamma_{ij}$ (lower left), the histogram for $\mathrm{Im}\zeta^\Gamma_{ij}$ (upper right), and the histogram for $|\zeta^\Gamma_{ij}|$ (lower right). The number of points in the histograms for each set is the lattice volume, V, of Table I. Note the logarithmic scale on the histogram plots. Red points and lines denote diagonal ζ^Γ_{ii}, and black off-diagonal ζ^Γ_{ij} ($j \neq i$). In the case of the vector overlap, $\Gamma = \gamma^\mu$, we separate the off-diagonal ζ^Γ_{ij} into two. Black is reserved for $|j| \neq |i|$ and the case of $j = -i$ is shown in blue.

The most striking feature for the scalar (Fig. 4) and pseudoscalar (Fig. 5) is how different the diagonal and off-diagonal distributions are. The diagonal scalar overlap ζ^1_{ii} is a sum of absolute squares, so it is real and positive. Because $f_{-i}(x) = \varepsilon(x) f_i(x)$ and the taste-singlet scalar operator is local, $\zeta^1_{i,-i}$ is equal to $\zeta^1_{i,i}$ on even sites but real and negative on odd sites. Upon averaging over a hypercube in Eq. (A1), cancellations render $\zeta^1_{i,-i}$ relatively small. It is visible on Fig. 4 as a black line stretching along the negative real axis; the positive part being invisible underneath the red line for $\zeta^1_{i,i}$. The off-diagonal ($|j| \neq |i|$) scalar overlap ζ^1_{ij} is a complex number of random phase. The width of all the histograms falls going

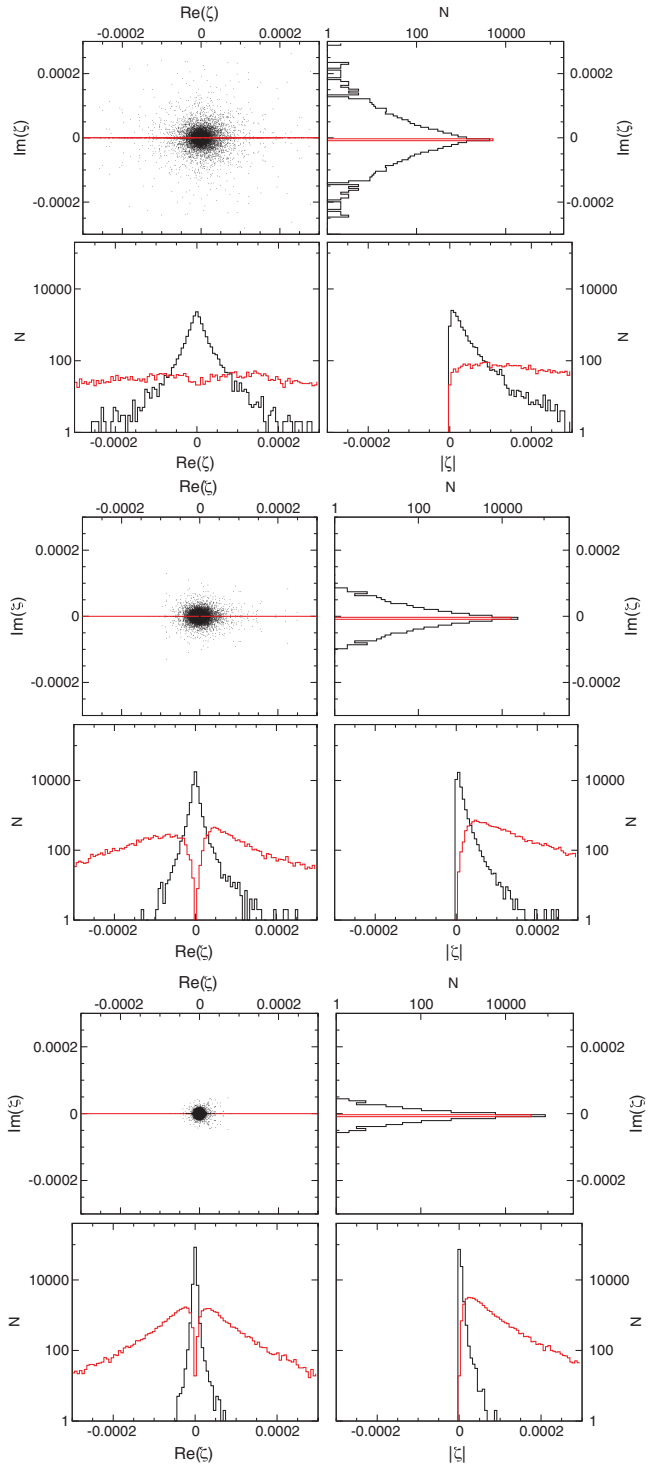

FIG. 5 (color). $\zeta_{ij}^{\gamma^5}$ on coarse (top), intermediate (middle), and fine (bottom) $|Q| = 1$ gluon field configurations, with $j = i$ (red) and $j \neq i$ (black), $i, j = \pm 1, \pm 2$. Note the logarithmic y-axis scale for the histograms.

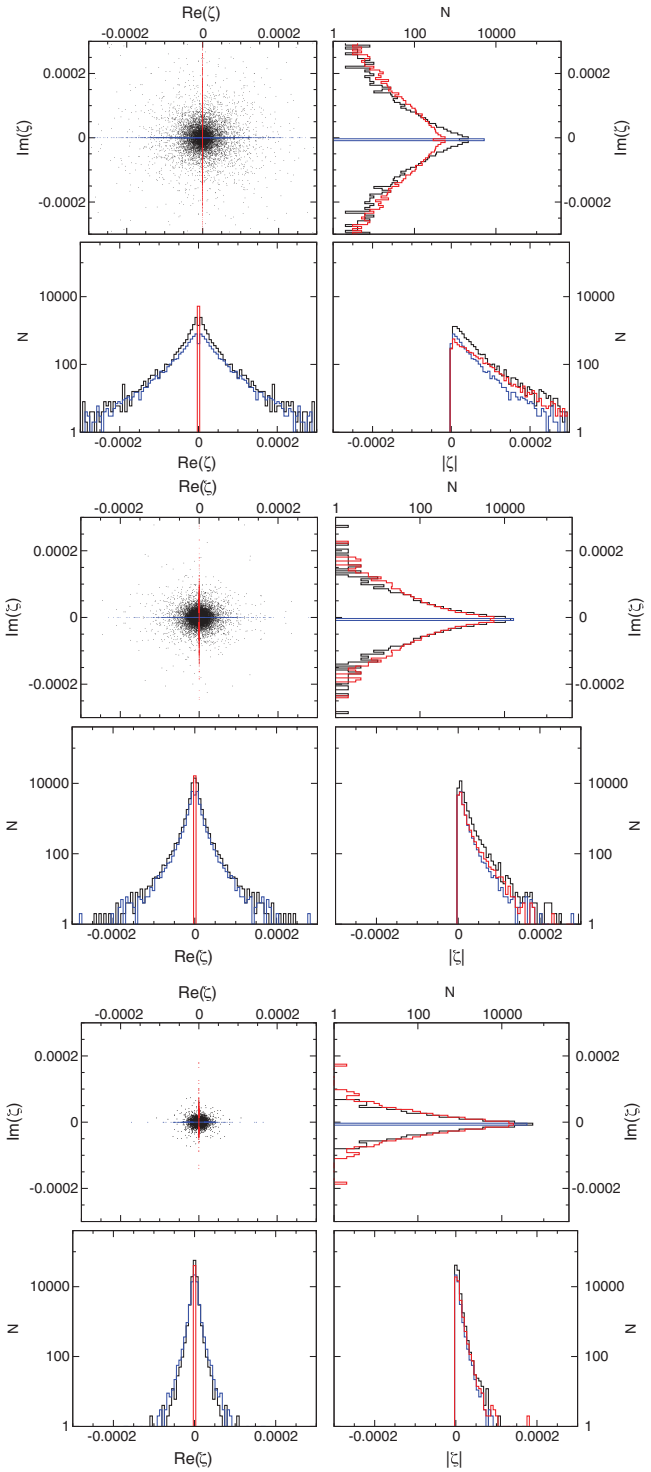

FIG. 6 (color). $\zeta_{ij}^{\gamma^\mu}$ on coarse (top), intermediate (middle), and fine (bottom) $|Q| = 1$ gluon field configurations, with $j = i$ (red), $j = -i$ (blue), and $|j| \neq |i|$ (black), $i, j = \pm 1, \pm 2$. Note the logarithmic y-axis scale for the histograms.

down the column of plots as the lattices become finer. What is crucial for the taste structure of the eigenvectors, however, is the relative width of the histograms for $|\zeta_{ij}^{\Gamma}|$ for $i \neq j$ compared to that for $|\zeta_{ii}^{\Gamma}|$. From the plots it can be seen that the width of the off-diagonal distribution is falling faster with lattice spacing than that of the diagonal. Figure 4 shows a single configuration with $|Q| = 1$, but we have examined others, and they look the same.

Figure 5 for the pseudoscalar case shows two configurations, one each with $Q = +1$ and -1. The plots behave in the same way as the scalar overlaps, except that $\zeta_{ii}^{\gamma^5}$ is real and *negative* for $Q = -1$, as a consequence of parity. From the same arguments as above, since the taste-singlet pseudoscalar operators links odd sites to odd sites and even sites to even sites, $\zeta_{i,-i}^{\gamma^5}$ is also real and takes the same or opposite sign to $\zeta_{i,i}^{\gamma^5}$ on odd sites or even sites. $\zeta_{i,-i}^{\gamma^5}$ is therefore not visible beneath $\zeta_{i,i}^{\gamma^5}$ on Fig. 5. Once again, looking down the plots, we see clearly that the width of the off-diagonal distribution (combining $j = -i$ and $|j| \neq |i|$) decreases with lattice spacing, relative to the diagonal distribution.

With $\zeta_{ij}^{\gamma^\mu}$ the behavior differs. Recall that $\zeta_{ij}^{\gamma^\mu}$ should vanish for all i, j, even $j = i$. As seen in Fig. 6, we find $\zeta_{ii}^{\gamma^\mu}$ to be pure imaginary, which follows from the definition of the operator γ_I^μ, Eq. (A2); we find $\zeta_{i,-i}^{\gamma^\mu}$ to be pure real, which follows by changing the sign of the odd pieces of $f_{-i}(x)$ relative to $f_i(x)$, because the vector operator couples even to odd sites and vice versa; and we find $\zeta_{ij}^{\gamma^\mu}$, $|j| \neq |i|$, to be complex and of random phase. In this case, however, the widths of all three distributions not only are the same (when nonzero) but also decrease with decreasing lattice spacing together. Indeed the widths of all $|\zeta_{ij}^{\gamma^\mu}|$ distributions are similar to the widths of the $|\zeta_{ij}^{1}|$ and $|\zeta_{ij}^{\gamma^5}|$ distributions, $j \neq i$.

To visualize the lattice-spacing dependence more directly, we plot in Fig. 7 the width of the ζ_{ij}^{Γ} distributions, appropriately normalized, vs a^2. The widths are defined by the central 66% of the data in the lower right histogram for $|\zeta_{ij}^{\Gamma}|$, but calculating this histogram for ten configurations instead of just one or two. The errors are estimated by comparing the widths for two subsets of five configurations. The values we obtain for the widths, and their errors, are given in Table II. Since the eigenvectors are normalized to have modulus 1 at each lattice spacing, the widths do not have a physical interpretation. The best that one can do is to normalize the off-diagonal widths against diagonal widths, as is appropriate for the test of Eq. (32). This ratio of widths is plotted for the scalar and pseudoscalar in Fig. 7. For the vector, we have no diagonal quantity that survives in the continuum limit, so we normalize instead against the diagonal pseudoscalar width. Although it is difficult to be quantitative (full ensemble averages of the widths are too costly, and the determination of the lattice spacing in the quenched approximation is ambiguous), the trend in Fig. 7 is clear and consistent with what is needed according to Eq. (32).

Figure 7 shows, with dashed lines, representative fits as a polynomial in a^2 to our results. The fits include a constant plus quadratic, quartic, and sixth powers of a. The slope of the nth polynomial term is constrained by a Bayesian prior to a size of $(1.0\ \mathrm{GeV})^n$ suggested by the slope of pion taste

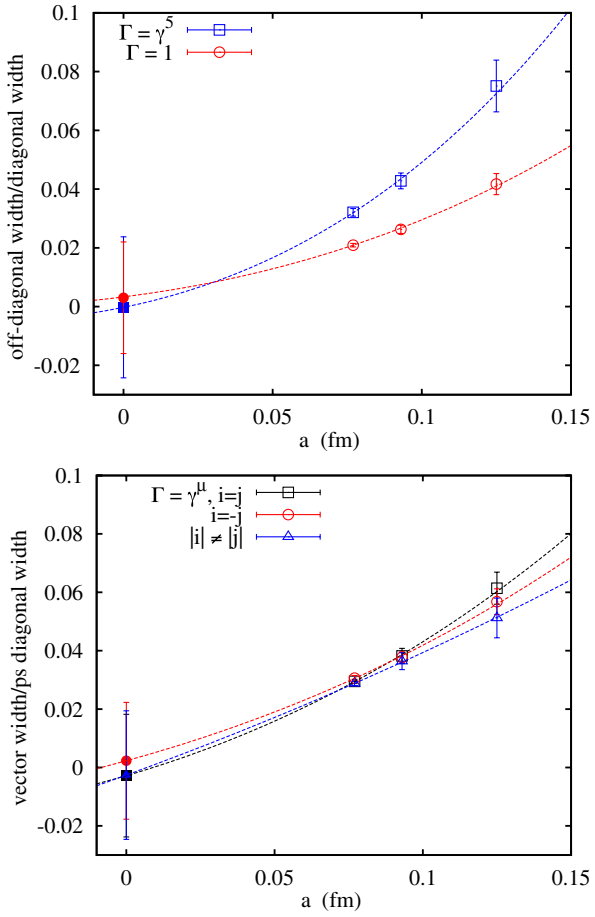

FIG. 7 (color online). The top plot shows the width of $|\zeta_{ij}^{\Gamma}|$, $j \neq i$, divided by the width of $|\zeta_{ii}^{\Gamma}|$, for $\Gamma = 1, \gamma^5, i, j = \pm 1, \pm 2$. The $\Gamma = 1$ case is given by open circles (red online), along with a representative polynomial fit in the square of the lattice spacing and the corresponding value in the continuum limit (filled circles). The equivalent results for $\Gamma = \gamma^5$ are given by open and closed squares (blue online). The lower plot shows the width of $|\zeta_{ij}^{\gamma^\mu}|$ divided by the width of $|\zeta_{ii}^{\gamma^5}|$ plotted against the lattice spacing. The case $i = j$ is given by (black) open and closed squares, the case $i = -j$ by (red) open and closed circles, and the case $|i| \neq |j|$ by (blue) open and closed triangles.

splittings [75]. It is very easy to obtain good fits with any combination of different polynomials, for example, including or not including a linear term, so it is not possible to say definitively what the lowest power of a is that appears in the a dependence of the ζ_{ij}. The solid points on the plots in Fig. 7 give the $a = 0$ value of the width ratios, compatible with zero in all cases. Thus, our results are consistent with the expectation in Eq. (32), although the data are not able to determine p_{ζ^Γ} in a definitive way.

We have also investigated the volume dependence of the ζ_{ij}^{Γ} for $i, j = \pm 1, \pm 2$ at the intermediate lattice spacing (i.e., on sets 2, 3, and 4), and these results are also included in Table II. We see that the widths again fall as the volume of the lattice increases. Naively this is simply a result of the

TABLE II. Widths, in lattice units and multiplied by 10^4, obtained for different $|\zeta_{ij}^{\Gamma}|$ histograms on each set of $|Q| = 1$ gauge configurations. The first column gives the set and then subsequent columns list the width, with an estimate of the error, for different Γ and i, j combinations, $i, j = \pm 1, \pm 2$.

Set	γ^5, $i = j$	γ^5, $i \neq j$	γ^μ, $i = j$	γ^μ, $i = -j$	γ^μ, $\|i\| \neq \|j\|$	1, $i = j$	1, $i \neq j$
1	3.93 (31)	0.296 (26)	0.242 (11)	0.202 (21)	0.224 (1)	6.84 (17)	0.285 (23)
2	4.08 (56)	0.180 (11)	0.188 (23)	0.146 (12)	0.155 (16)	6.07 (70)	0.158 (9)
3	1.49 (3)	0.0635 (38)	0.0567 (36)	0.0541 (42)	0.0561 (22)	2.15 (6)	0.0566 (27)
4	0.548 (26)	0.0390 (16)	0.0242 (10)	0.0246 (17)	0.0219 (5)	0.846 (29)	0.0406 (22)
5	0.716 (14)	0.0230 (7)	0.0211 (2)	0.0206 (2)	0.0219 (5)	0.954 (16)	0.0199 (5)

normalization of the eigenvectors to 1 over an increasing number of lattice sites. Indeed the widths do seem to have simple behavior, inversely proportional to $1/V$, at least for the diagonal scalar and pseudoscalar widths and the vector widths. Note that this is not inconsistent with the fact that, for example, the very high values of the pseudoscalar diagonal overlaps are localized around the instantons that give rise to the near-zero modes.

The pseudoscalar and scalar widths behave quite differently as a function of lattice spacing than they do as a function of volume. We can see this by comparing the histograms in Fig. 8 for ζ_{ij}^{Γ} on the fine lattices, set 5, and the large intermediate volume lattices, set 4. Both of these have 20^4 lattice points. We see that the diagonal distribution is broader on the finer lattices and the off-diagonal distribution markedly narrower, consistent with the fairly rapid fall with lattice spacing of the ratio of the widths seen in Fig. 7. For the vector case, as is clear from Table II, the behavior of the widths with the lattice spacing is only slightly steeper than that with volume. However, this still represents a fall to zero with lattice spacing when compared to the diagonal scalar and pseudoscalar overlaps which survive the continuum limit, as we see in Fig. 7.

We have not shown histograms for the axial vector or tensor operators. We have looked at these operators in terms of the relevant meson correlators (see the following subsections) and they give qualitatively identical results to the vector and scalar/pseudoscalar cases, respectively. It therefore seems unlikely that they would upset the picture gleaned here.

D. Flavor-singlet meson correlators

Our results in Sec. IV C show how the taste-singlet overlaps, $\zeta_{ij}^{\Gamma}(x)$, of different near-zero-mode eigenvectors behave as expected to give the correct continuum behavior for the 't Hooft vertex. Here we show explicitly how this translates into the correct continuum behavior for the near-zero mode contribution to the flavor-singlet meson correlator. We also look at nonzero-mode contributions, as well as flavor-nonsinglet correlators, wherever they are useful to fill out the picture obtained. As discussed in Sec. III it is sufficient to work in the quenched approximation since the structural issue of the behavior of the eigenvector overlaps—in a fixed-$|Q|$ sector—is the same whether sea quarks are included or not.

To relate results as closely as possible to those of a complete meson correlator calculation in lattice QCD, we consider meson correlators projected onto zero spatial momentum by summing over spatial sites. This leads us to consider a modification of the eigenvector overlaps

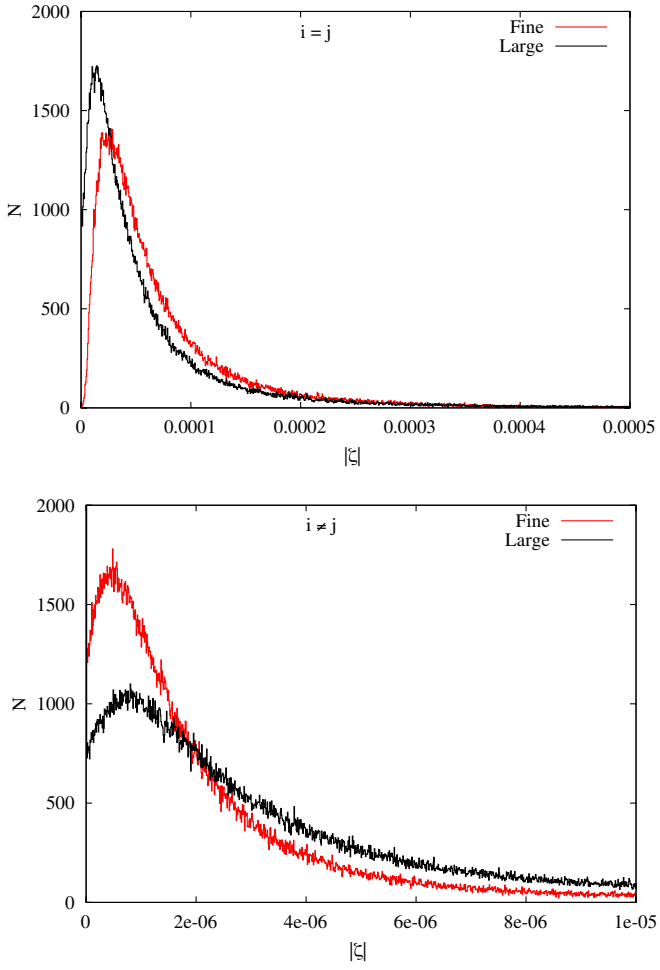

FIG. 8 (color online). Histogram of $|\zeta_{ij}^{\gamma^5}|$, for $i = j$ (top) and $i \neq j$ (bottom), comparing results on the fine lattice (set 5—red/gray) and the large intermediate lattice (set 4—black).

$$\bar{\zeta}^{\Gamma}_{rs}(t) = \sum_{\boldsymbol{x}} f^{\dagger}_r(\boldsymbol{x}, t)\Gamma_I f_s(\boldsymbol{x}, t), \tag{44}$$

summing over a time slice instead of a 2^4 hypercube. Then the zero-momentum connected and disconnected contributions can be constructed, as in Eqs. (40) and (41) from correlations of time slice overlaps

$$X^{\Gamma}_{rs}(T) = \sum_t \bar{\zeta}^{\Gamma}_{rs}(t)\bar{\zeta}^{\Gamma}_{sr}(t+T), \tag{45}$$

$$Y^{\Gamma}_{rs}(T) = \sum_t \bar{\zeta}^{\Gamma}_{rr}(t)\bar{\zeta}^{\Gamma}_{ss}(t+T). \tag{46}$$

Note that $X^{\Gamma}_{rr}(T) = Y^{\Gamma}_{rr}(T)$ by construction, and we consider values for r, s that correspond to nonzero modes as well as near-zero modes.

The full connected correlator is $C(T) = \sum_{\boldsymbol{x},\boldsymbol{y}} C(\boldsymbol{x}, t; \boldsymbol{y}, t+T)$, with $C(x, y)$ defined in Eq. (35). Similarly, the disconnected correlator is $D(T) = \sum_{\boldsymbol{x},\boldsymbol{y}} D(\boldsymbol{x}, t; \boldsymbol{y}, t+T)$, following Eq. (36). $C(T)$ is then made up of X_{rs} correlated overlaps (on the quenched configurations that we are studying) as

$$C(T) = \langle \mathcal{C}(T)\rangle_U = \sum_{r,s}\left\langle \frac{X_{rs}(T)}{(i\lambda_r + m)(i\lambda_s + m)}\right\rangle_U, \tag{47}$$

where we have made explicit the dependence on the eigenvalues in the denominator. For $D(T)$ we have

$$D(T) = \langle \mathcal{D}(T)\rangle_U = \sum_{r,s}\left\langle \frac{Y_{rs}(T)}{(i\lambda_r + m)(i\lambda_s + m)}\right\rangle_U. \tag{48}$$

The disconnected correlator factorizes into the product of sums over diagonal overlaps $\bar{\zeta}^{\Gamma}_{rr}$, but the connected correlator contains overlaps between different eigenvectors.

Note that the factor $|m|\mathbb{D}'$ of Eqs. (35) and (36) from the $n_f = 1$ sea quark determinant is missing. This affects the weighting of the particular configurations in the ensemble and therefore the quantitative results obtained for $C(T)$ and $D(T)$. However, it does not affect qualitatively the properties of the X_{rs} factors that we demonstrate here, which are evident in a fixed-$|Q|$ sector and even, in some cases, on a configuration-by-configuration basis in their contribution to $\mathcal{C}(T)$ and $\mathcal{D}(T)$.

As discussed in Sec. III, we then have to test whether the near-zero modes give rise to a divergence in the correlator for flavor-singlet meson H as $m \to 0$, when the connected and disconnected contributions are combined with their appropriate taste factors of 4 and 16 [Eq. (34)]:

$$M^H(T) = \langle \mathcal{M}^H(T)\rangle_U = \frac{1}{4}C^H(T) - \frac{1}{16}D^H(T). \tag{49}$$

To obtain a finite result as $m \to 0$ for $M(T)$ we need the near-zero-mode contributions to cancel between $C(T)$ and $D(T)$. This in turn requires the off-diagonal correlated overlaps, X_{ij}, $i \neq j$, between different near-zero eigenvectors in the same staggered eigenvalue quartet to vanish in the continuum limit. Then each quartet behaves as four copies of a single mode and, including the factors of $1/4$ and $1/16$, reproduces within $M(T)$ the behavior expected of eigenmodes of the Dirac operator in the continuum. We show how this works explicitly for the examples of scalar, pseudoscalar, (axial) vector, and tensor mesons in the following subsections. We do this with the same $|Q| = 1$ quenched configurations used in the previous subsection. The correlator results are, however, averaged over all $|Q| = 1$ configurations for each ensemble, rather than just 10.

1. Flavor-singlet pseudoscalar mesons

We first discuss the important case of the calculation of the flavor-singlet pseudoscalar meson (η') correlator, and the associated case of the flavor-nonsinglet meson (π) correlator. In continuum QCD with, say, two equal mass light quarks, this is readily analyzed in terms of the eigenvectors and eigenvalues of the massless Dirac matrix. For $|Q| = 1$ gluon field configurations there is one zero mode with a chirality $\phi_0^{\dagger}\gamma_5\phi_0 = \pm 1$. The π meson correlator has no disconnected contribution and the connected contribution is readily seen to obey, on a given gluon field configuration,

$$\sum_T \mathcal{M}^{\pi}(T) = \sum_{\sigma}\frac{1}{\lambda_\sigma^2 + m^2}, \tag{50}$$

where m is the quark mass and the sum is over all eigenmodes of the massless Dirac matrix, including the zero mode. Each eigenmode contributes a correlated overlap of 1 when summed over T. For the zero mode, this comes from the square of the chirality. The nonzero modes have chirality zero but still contribute a correlated overlap factor of 1 because the γ_5 matrix connects the modes σ and $-\sigma$ with $\lambda_{-\sigma} = -\lambda_\sigma$. Then (continuum) $\sum_t \bar{\zeta}^{\gamma_5}_{\sigma,-\sigma}(t) = 1$ from eigenfunction normalization.

The η' meson correlator is made from the same eigenvectors but now has a disconnected contribution coming from the zero mode that exactly cancels the zero-mode contribution to the connected correlator. Thus, on a given configuration,

$$\sum_T \mathcal{M}^{\eta'}(T) = \sum_{\sigma\neq 0}\frac{1}{\lambda_\sigma^2 + m^2}. \tag{51}$$

There is now no contribution from the zero mode and the correlator is finite as $m \to 0$. This continues to be true on averaging over gauge fields and including determinant factors.

Now let us show how staggered fermions reproduce Eqs. (50) and (51). For the Goldstone π meson correlator, it is straightforward and mechanical. Then $\Gamma = \gamma_P^5 = \varepsilon(x)$ connects eigenvectors f_s and f_{-s}, and the correlated overlap contribution is again 1, when summed over T, simply from eigenvector normalization. The difference with the

continuum case is that this is *also* true for the near-zero modes. Thus, we obtain an equation very similar to that in the continuum on a single gluon field configuration:

$$\sum_T \mathcal{M}^\pi(T) = \frac{1}{4}\sum_s \frac{1}{\lambda_s^2 + m^2} = \sum_q \frac{1}{\bar{\lambda}_q^2 + m^2} + \mathrm{O}(a^2), \quad (52)$$

where s is a sum over all modes *including* the near-zero modes and the factor of $1/4$ is the same as in Eqs. (34) and (49). Since the staggered eigenvalues come in quartets that become degenerate in the $a \to 0$ limit, the lower equation replaces the four eigenvalues in a quartet by their mean square and sums all quartets, q, including the near-zero-mode quartet. This then clearly reproduces the continuum Eq. (50) as $a \to 0$.

The flavor-singlet correlator is constructed differently and includes both connected and disconnected contributions. With staggered fermions, we must use the flavor-taste-singlet pseudoscalar, $\Gamma = \gamma_I^5$. In demonstrating that Eq. (51) is reproduced, we also show that the correlated overlaps behave so as to give a finite result for the η' correlator.

From our earlier results on chirality, we can anticipate what the disconnected correlated overlaps $Y_{ij}^{\gamma^5}$ look like. Because $\sum_t \bar{\xi}_s^{\gamma^5}(t) = \mathcal{X}_s$ we expect the large values of $Y_{ij}^{\gamma^5}$ to be those that involve the near-zero modes with their large-chirality values. Indeed

$$\sum_T Y_{ij}^{\gamma^5}(T) = \mathcal{X}_i \mathcal{X}_j. \quad (53)$$

This expectation is borne out by the numerical results. On averaging over $|Q| = 1$ gauge fields, $Y_{11}^{\gamma^5}$, $Y_{22}^{\gamma^5}$, and $Y_{12}^{\gamma^5}$ are all equal, being the "typical" product of overlaps for two near-zero modes. $\langle Y_{11}^{\gamma^5}\rangle_{|Q|=1}$ is shown as a function of T in Fig. 9. Results for modes -1 and -2 from the near-zero-mode quartet match these because, as discussed above, the chirality of mode -1 is identical to that of 1 and -2 to that of 2. Thus, the sum over all the zero modes, $i, j \in \{\pm 1, \pm 2\}$, of $Y_{ij}^{\gamma^5}$ gives $4 \times 4 = 16$ times the square of the chirality for a typical zero mode. This is divided by 16 in the contribution to the disconnected correlator, as in Eq. (49), and so the contribution becomes exactly what is required to match that from the one zero mode for continuum quarks, up to a renormalization factor for the taste-singlet pseudoscalar current.

The nonzero modes, for example, mode 3, have small chirality and therefore $Y_{33}^{\gamma^5}$ is small, as also shown in Fig. 9. In the continuum this would be zero. Here it is not zero for nonzero lattice spacing but tends to zero as $a \to 0$. In fact, because we find that $Y_{rr} = Y_{ss} = Y_{rs}$ for modes in the nonzero-mode quartet, $r, s \in \{3, 4, 5, 6\}$, then the total contribution from the quartet, when divided by 16, cancels against the contribution from $X_{rr}^{\gamma^5}$ divided by 4 in the total

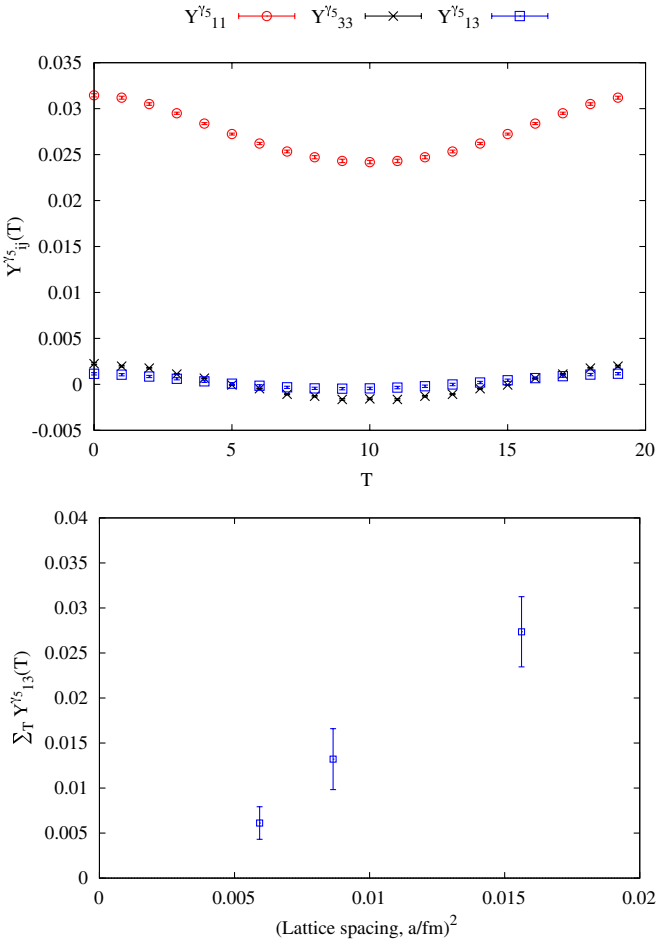

FIG. 9 (color online). Diagonal and off-diagonal correlated overlaps $Y_{ij}^{\gamma^5}(T)$ between eigenvectors 1 and 3 that contribute to the disconnected piece of the η' correlator at zero spatial momentum. Results are given for the average over $|Q| = 1$ configurations in the fine ensemble, set 5. The lower plot shows the off-diagonal correlated overlap summed over time separation as a function of the square of the lattice spacing.

pseudoscalar flavor-singlet correlator, as for the near-zero-mode quartet.

It is also worth discussing the cross term $Y_{13}^{\gamma^5}$ between the near-zero-mode quartet and the nonzero-mode quartet since this would also be identically zero in the continuum. Figure 9 shows the results for $Y_{13}^{\gamma^5}(T)$, which, summed over T, has a value which is the square root of the product of the sums over T of $Y_{11}^{\gamma^5}$ and $Y_{33}^{\gamma^5}$. The lower plot of Fig. 9 then shows explicitly how $\sum_T Y_{13}^{\gamma^5}(T)$ vanishes as $a \to 0$. Similar behavior is seen for other terms that are related to the chirality of nonzero modes.

For X^{γ^5} the results for the diagonal case are the same as for Y^{γ^5}. The results for the off-diagonal X^{γ^5} are less clear *a priori*. In fact, we find in all cases that the off-diagonal correlated overlaps within a quartet are zero when averaged over gauge fields. Figure 10 illustrates this for

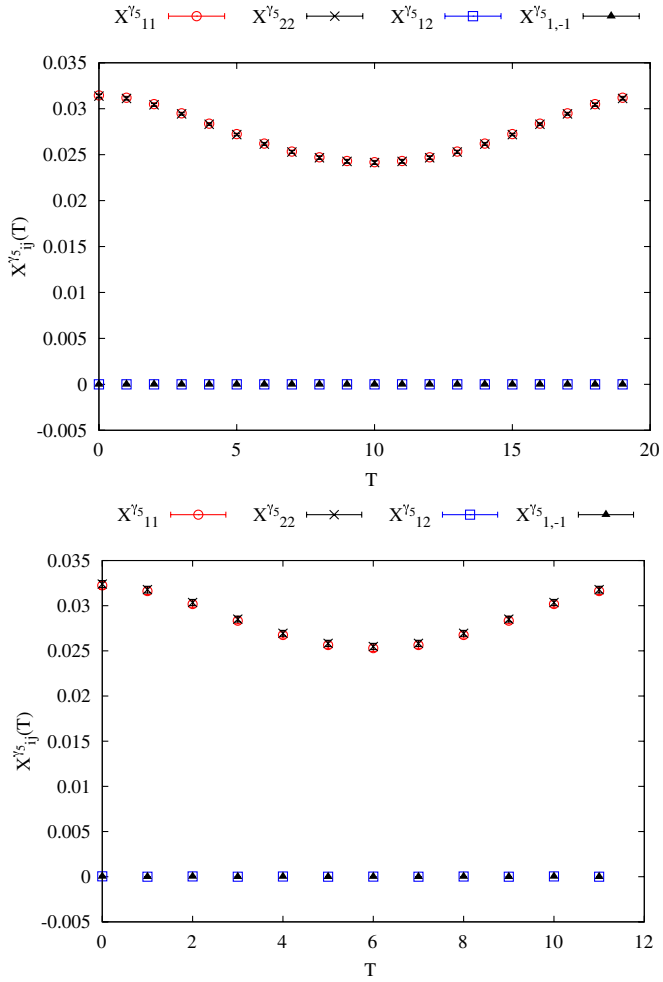

FIG. 10 (color online). The correlated overlaps $X^{\gamma^5}_{ij}(T)$ between near-zero modes 1, 2, and -1 that contribute to the connected piece of the η' correlator at zero spatial momentum. Results are given for the average over $|Q| = 1$ configurations in the fine ensemble, set 5 (top) and the coarse ensemble, set 1 (bottom).

modes 1 and 2 in the near-zero-mode quartet. $X^{\gamma^5}_{11}$ and $X^{\gamma^5}_{22}$ are large (being equal to $Y^{\gamma^5}_{11}$ and $Y^{\gamma^5}_{22}$) but $X^{\gamma^5}_{12}$ has an average of zero. The same results are obtained for the -1 and -2 modes. We also see an average of zero for the correlated overlaps between the positive and negative eigenmodes within the quartet. This is illustrated for $X^{\gamma^5}_{1,-1}$ in Fig. 10. $X^{\gamma^5}_{1,-2}$ is very similar.

The size of correlated overlaps changes very little with the lattice spacing. Figure 10 also compares correlated overlaps $X^{\gamma^5}_{ij}$ on the coarsest lattices, set 1, with those for the finest lattices, set 5.

An average of zero is also seen for off-diagonal terms between modes in the first nonzero-mode quartet and between modes in the near-zero-mode quartet and modes in the first nonzero-mode quartet. These points are illustrated in Fig. 11.

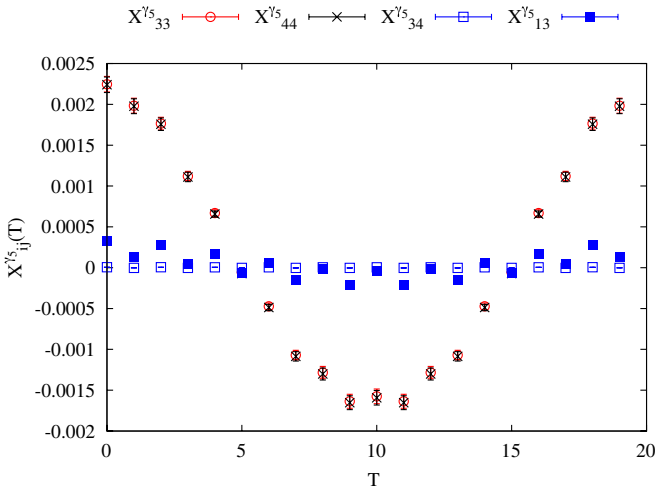

FIG. 11 (color online). The correlated overlaps $X^{\gamma^5}_{rs}(T)$ between nonzero modes 3 and 4 that contribute to the connected piece of the η' correlator at zero spatial momentum. Results are given for the average over $|Q| = 1$ configurations in the fine ensemble, set 5. Results are also shown for the correlated overlap between near-zero mode 1 and nonzero mode 3.

To understand $X^{\gamma^5}_{rs}$ more completely, we must also study correlated overlaps between positive and negative nonzero eigenmodes. Although this is not relevant to the behavior of the 't Hooft vertex, it shows very clearly how the connected contribution to the η' correlator becomes equal to that of the π meson in the continuum limit, up to a renormalization factor that arises because the taste-singlet pseudoscalar current is not absolutely normalized.

Figure 12 shows the correlated overlaps, $X^{\gamma^5}_{rs}$, between the mode $r = 3$ and all the negative modes that correspond to the first negative nonzero quartet (which is the U_ε

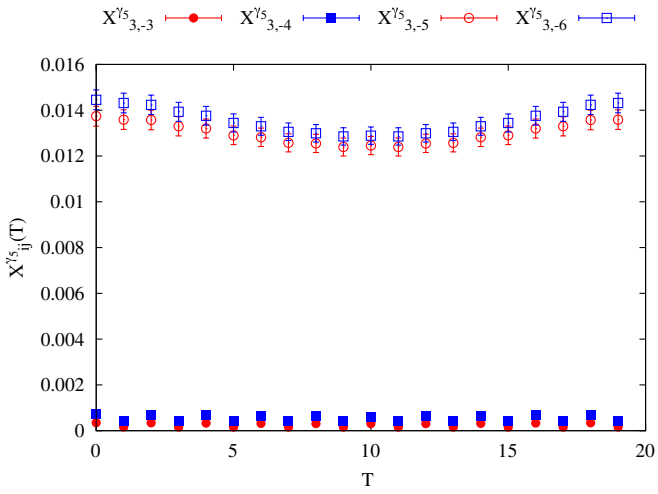

FIG. 12 (color online). The correlated overlaps $X^{\gamma^5}_{rs}(T)$ between nonzero mode 3 and modes -3, -4, -5, and -6 from its U_ε mirror quartet. Results are averaged over $|Q| = 1$ configurations for set 5.

"mirror" of the first positive nonzero quartet), i.e., $s = -3$, -4, -5, and -6. Interestingly, the correlated overlaps that are nonzero here are $X^{\gamma^5}_{3,-5}$ and $X^{\gamma^5}_{3,-6}$. These are equal and each about half the size of $X^{\gamma^5}_{1,1} = Y^{\gamma^5}_{1,1}$ (compare Figs. 10 and 12). Likewise, the nonzero correlated overlap for $r = 5$ appears with $s = -3$ and -4 having the same size as $X^{\gamma^5}_{3s}$, $s = -5, -6$. The correlated overlaps $X^{\gamma^5}_{4s}$ and $X^{\gamma^5}_{6s}$ show the corresponding pattern. Note the parallel with what happens in the case of the near-zero-mode quartet, where $X^{\gamma^5}_{1,-1}$ and $X^{\gamma^5}_{1,-2}$ tend to zero (as shown in Fig. 10), and $X^{\gamma^5}_{3,-3}$ and $X^{\gamma^5}_{3,-4}$ tend to zero too. The difference here is that another pair belongs to the mirror quartet, whereas 1, 2, -1, and -2 form a single quartet that is its own mirror. The pattern seen in Fig. 12 is repeated for other nonzero-mode quartets. For example, $X^{\gamma^5}_{7,-9}$ and $X^{\gamma^5}_{7,-10} \approx 0.014$, while $X^{\gamma^5}_{7,-7}$ and $X^{\gamma^5}_{7,-8}$ are much much smaller.

Thus, the large contributions from nonzero modes to the connected correlator for the taste-singlet pseudoscalar meson come from correlated overlaps connecting members of a quartet and members of its mirror quartet, in fact members of the opposite pair of the mirror quartet. When these correlated overlaps are summed over a quartet they give a result, per quartet member, approximately equal to that of a typical near-zero-mode contribution. The near-zero-mode contributions, on the other hand, come from diagonal terms, as a result of nonzero chirality. On adding all modes together, as in Eq. (47), and dividing by 4 we obtain a result per quartet, similar to that in Eqs. (50) and (52). The way in which this is achieved is rather different from that for the Goldstone π meson, and the different mode contributions follow more closely that of the continuum. A difference with both the continuum and the staggered Goldstone π is that there is a constant of proportionality which is the square of the chirality of the zero modes. The disconnected terms cancel all diagonal connected contributions (having in fact the same constant of proportionality), and therefore we finally obtain, for the η' correlator, a result that tends to Eq. (51) in the continuum limit, once the taste-singlet pseudoscalar current is appropriately normalized.

Let us now demonstrate the cancellation between the connected and disconnected contributions from the near-zero modes more explicitly. Figure 13 shows histograms in the $|Q| = 1$ sector for

$$\sum_{i,j=\pm1,\pm2} -\frac{X^{\gamma^5}_{ij}(T)}{4} + \frac{Y^{\gamma^5}_{ij}(T)}{16}, \tag{54}$$

evaluated at the midpoint of the lattice, $T = T_{\rm mid}$ for the three sets—1, 3, and 5—that have the same physical volume but different lattice spacings. Then $T_{\rm mid}$ corresponds approximately to the same physical time separation in each case. From Fig. 13, it is clear that this combination of X and Y, which skeptics have worried could be troublesome, is in fact zero on average at every value of the lattice spacing. The histogram of values shows that the distribution is somewhat broader on the coarser lattices, but there is no other effect from the lattice spacing.

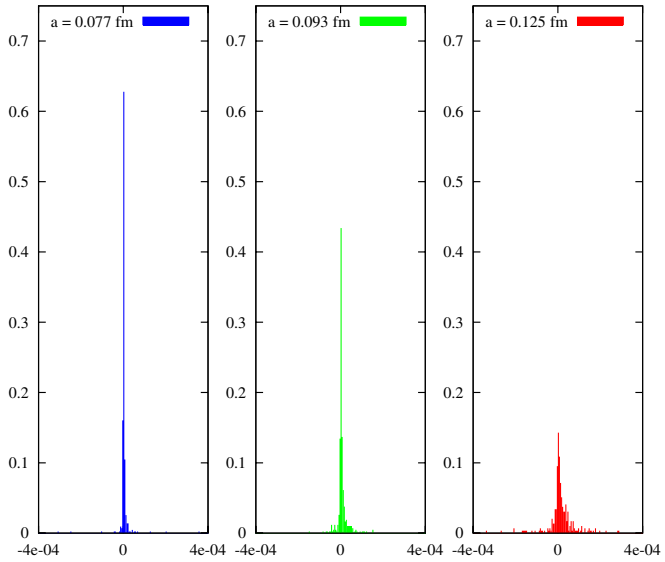

FIG. 13 (color online). A histogram of values of the combination $-X(T_{\rm mid})/4 + Y(T_{\rm mid})/16$ calculated from the near-zero modes $i, j = \pm1, \pm2$ for the $|Q| = 1$ configurations for sets 1, 3, and 5. The results are plotted for time separation, $T_{\rm mid}$, set to the midpoint of the lattice.

In the above discussion, we have focused on the $|Q| = 1$ case because that is the easiest one with which to study near-zero and nonzero modes. However, results on configurations with other Q values also behave exactly as expected from this picture. Figure 14 shows results for correlated overlaps $X^{\gamma^5}_{ij}$ for 27 configurations with $|Q| = 2$ from the finest, set 5 lattices. The correlated overlaps are between modes 1 and 3 which are now members of two separate near-zero-mode quartets. We see that there is negligible correlated overlap between modes from different near-zero quartets, so the counting for each quartet, taken care of by the subsequent division by 4 for the connected contribution, is exactly as for the $|Q| = 1$ case.

2. Flavor-singlet scalar mesons

The flavor-singlet scalar case is easy to analyze both in the continuum and for staggered fermions because of the simple form of the taste-singlet scalar, $\Gamma = 1_I$. The orthogonality and normalization of the eigenvectors give $\sum_I \bar{\zeta}^1_{rs}(t) = \delta_{rs}$. Thus, the disconnected contribution in the continuum becomes

$$\sum_T \mathcal{D}^\sigma(T) = \sum_{r,s} \frac{1}{(i\lambda_r + m)(i\lambda_s + m)}, \tag{55}$$

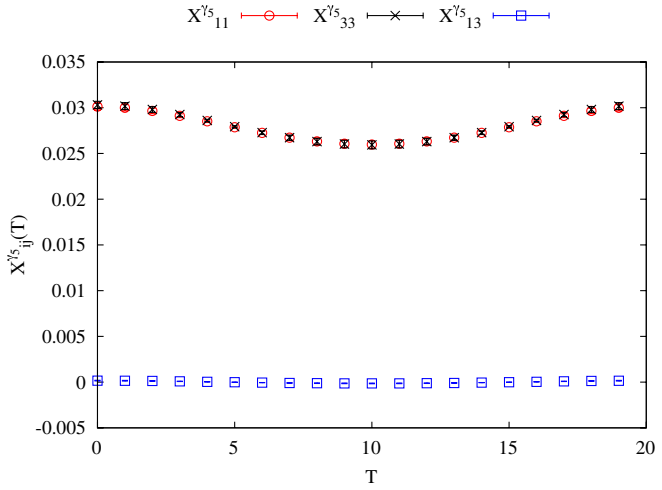

FIG. 14 (color online). Overlaps $X_{ij}^{\gamma^5}$ averaged over the 27 lattices from the finest ensemble, set 5, that had topological charge $|Q| = 2$. Results are shown for mode 1 from the first near-zero-mode quartet and mode 3 from the second near-zero-mode quartet.

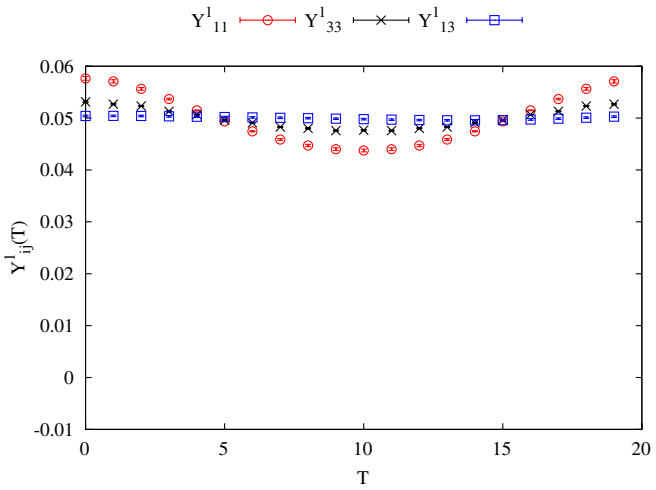

FIG. 15 (color online). Diagonal and off-diagonal correlated overlaps $Y_{rs}^1(T)$ between eigenvectors 1 and 3 that contribute to the disconnected piece of the flavor-singlet scalar meson correlator at zero spatial momentum. Results are given for the average over $|Q| = 1$ configurations in the fine ensemble, set 5.

where the sum is over all eigenmodes. The connected contribution is

$$\sum_T \mathcal{C}^\sigma(T) = \sum_r \frac{1}{(i\lambda_r + m)^2} \tag{56}$$

and we see that it is canceled by diagonal terms from Eq. (55). In particular, for $|Q| = 1$, the single zero-mode contribution to the total flavor-singlet correlator cancels between $\mathcal{D}$ and $\mathcal{C}$ to give a finite result for $\mathcal{M}^\sigma$ as $m \to 0$. For staggered fermions, Eqs. (55) and (56) still hold, with a sum over the total number of eigenmodes. By taking a suitable average over the eigenvalues in a quartet, the cancellation of diagonal terms quartet by quartet mimics that of the continuum. In particular, neglecting the near-zero λ_i relative to m and dividing $\mathcal{C}$ by 4 and $\mathcal{D}$ by 16, it is clear that exactly the same cancellation of the contributions from the near-zero-mode quartet occurs as in the continuum.

Figures 15 and 16 show a representative sample of Y_{rs}^1 and X_{rs}^1, plotted as a function of T for set 5. Figure 15 shows correlated overlaps Y_{11}^1 for a near-zero mode and Y_{33}^1 for a nonzero mode as well as the off-diagonal Y_{13}^1. Set 5 lattices have a time extent of 20, so we expect values around 0.05, such that the sum over T yields 1. The results for all members of the near-zero-mode quartet agree with those of Y_{11}^1 and those of the first nonzero-mode quartet agree with those of Y_{33}^1. Unlike the pseudoscalar case, Y_{13}^1 is not zero but as large as Y_{11}^1 and Y_{33}^1 since $\sum_T Y_{rs}^1(T) = 1$ for all r, s both in the continuum and on the lattice.

Figure 16 shows the correlated overlaps $X_{rs}^1(T)$. Here $\sum_T X_{rs}^1(T) = \delta_{rs}$, and it is clear that the diagonal correlated overlaps are the same as those of the appropriate Y_{rs}^1 and the off-diagonal correlated overlaps are zero in each case.

Further detail is shown in Fig. 17, which gives the X_{rs}^1 between nonzero modes in mirror quartets. and between the positive and negative eigenmodes of the zero-mode quartet. Some of these correlated overlaps are large in the pseudoscalar case. None of them is large here and all yield zero after summing over T. Quite different behavior is seen in the different correlated overlaps, however. In particular, we see once again in these correlated overlaps the distinction between different pairs in the nonzero-mode quartets.

Figure 18 shows histograms in the $|Q| = 1$ sector for

$$\sum_{i,j=\pm1,\pm2} -\frac{X_{ij}^1(T)}{4} + \frac{Y_{ij}^1(T)}{16}, \tag{57}$$

evaluated at T_{mid} for the three sets—1, 3, and 5—that have the same physical volume but different lattice spacings. From Fig. 18, it is clear that, as in the pseudoscalar case, this combination of X and Y, which corresponds to the potentially divergent contribution of the near-zero modes to the scalar meson correlator, again actually vanishes on average at every value of the lattice spacing. The width of the histogram distribution is the quantity which changes with lattice spacing, becoming more narrowly peaked around zero as the lattice spacing goes to zero.

3. Flavor-singlet vector, axial vector, and tensor mesons

The correlated overlaps for the flavor-singlet tensor case behave similarly to the pseudoscalar and scalar. No simple analysis of correlated overlaps in terms of the chirality or normalization of the modes is possible and, indeed, we find

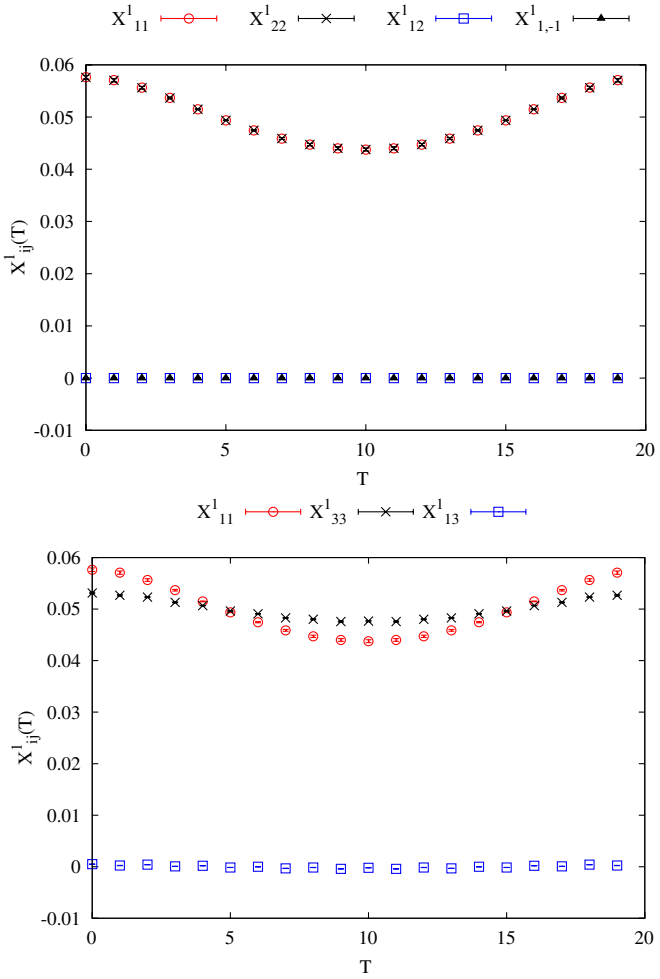

FIG. 16 (color online). The correlated overlaps $X^1_{rs}(T)$ between near-zero modes 1, 2, and -1 (top) and between near-zero mode 1 and nonzero mode 3 (bottom) that contribute to the connected piece of the flavor-singlet scalar meson correlator at zero spatial momentum. Results are given for the average over $|Q| = 1$ configurations in the fine ensemble, set 5.

that none of the correlated overlaps is large. Figure 19 shows that the key requirement for a sensible flavor-singlet correlator holds, i.e., that the off-diagonal correlated overlaps between different members of the near-zero-mode quartet are consistent with zero. This means, as above, that the connected and disconnected near-zero-mode contributions cancel rather than giving a potentially divergent piece.

The flavor-singlet vector and axial-vector cases behave somewhat differently, which can be traced back to the fact that the taste-singlet versions of these operators couple even and odd lattice sites together rather than even-to-even or odd-to-odd as with the other examples. The axial vector and vector behave in the same way, so we only show results here for the vector case. As discussed in Sec. III, in the continuum there is no zero-mode contribution to the disconnected piece of the flavor-singlet vector meson

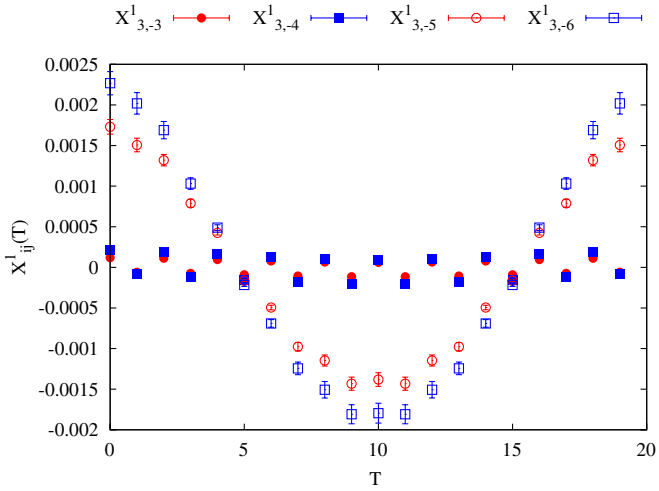

FIG. 17 (color online). The correlated overlaps $X^1_{rs}(T)$ between nonzero mode 3 and modes -3, -4, -5, and -6 from its mirror quartet. Results are averaged over $|Q| = 1$ configurations for set 5.

correlator because γ^μ and γ^5 anticommute. We show in Fig. 20 how this works for staggered fermions. Because $\bar{\zeta}^{\gamma^\mu}_{ii}$ couples odd and even sites, and f_{-1} has the opposite sign on odd sites to f_1, then $\bar{\zeta}^{\gamma^\mu}_{11}$ and $\bar{\zeta}^{\gamma^\mu}_{-1-1}$ have opposite sign. This means that the near-zero-mode contribution to the disconnected correlator from $Y^{\gamma^\mu}_{11}$ has opposite sign to that from $Y^{\gamma^\mu}_{1-1}$. This is seen clearly for $\mu = x$ in Fig. 20. Summing over $i, j \in \{\pm 1, \pm 2\}$ then clearly gives a total disconnected contribution to the flavor-singlet vector meson correlator of zero.

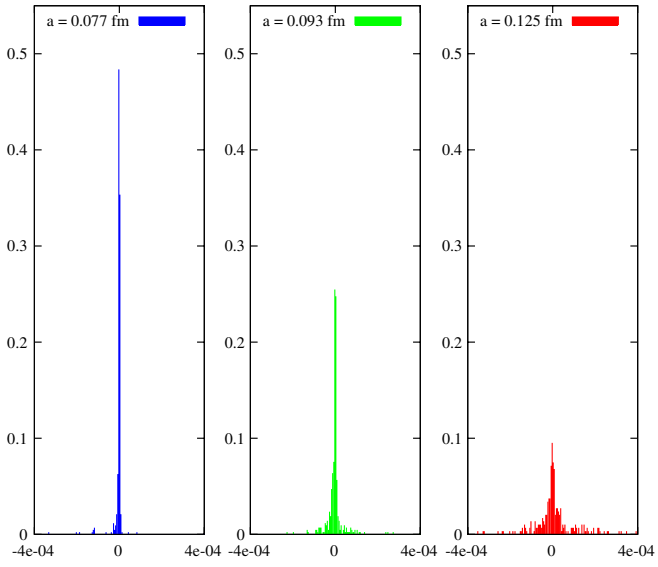

FIG. 18 (color online). A histogram of values of the combination $-X^1(T_{\rm mid})/4 + Y^1(T_{\rm mid})/16$ calculated from the near-zero modes for the $|Q| = 1$ configurations for sets 1, 3, and 5. The results are plotted for time separation set to the midpoint of the lattice, $T_{\rm mid}$.

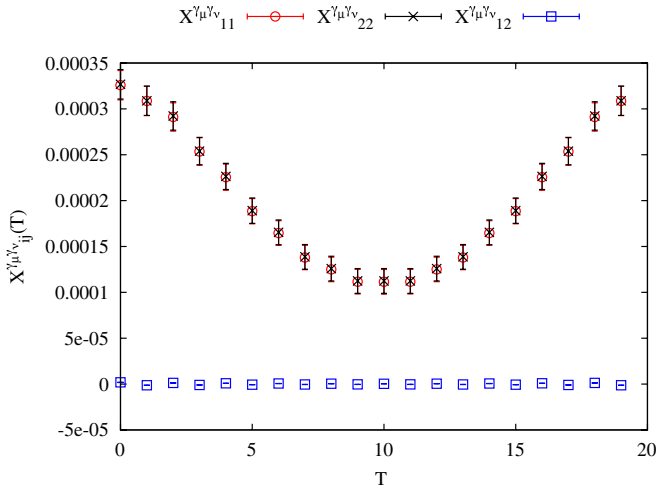

FIG. 19 (color online). The correlated overlaps $X_{ij}^{\sigma^{xy}}(T)$ between near-zero modes 1 and 2 that contribute to the connected piece of the flavor-singlet tensor meson correlator at zero spatial momentum. Results are given for the average over $|Q| = 1$ configurations in the fine ensemble, set 5.

The connected contributions are not zero time slice by time slice, as we see from Fig. 21. Correlated overlaps $X_{ii}^{\gamma^\mu}$ (equal to their counterparts $Y_{ii}^{\gamma^\mu}$ in Fig. 20) become pure oscillations, $(-1)^T$, that cancel upon summing over T. Oscillatory terms are a feature of staggered meson correlators, stemming from opposite-parity contributions to the correlator and, ultimately, the remaining time doubling. They do not then affect the properties of the ground state meson, in this case the flavor-singlet vector meson. The off-diagonal $X_{ij}^{\gamma^\mu}$ are close to zero and also oscillatory. Thus, once again there is no significant net contribution from near-zero modes to the flavor-singlet vector meson.

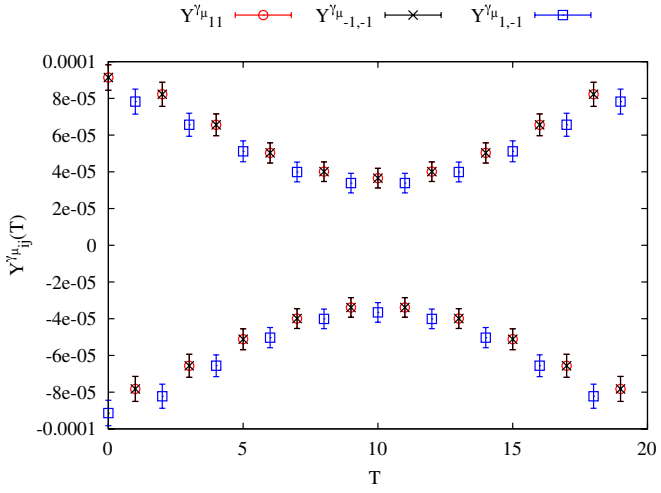

FIG. 20 (color online). The correlated overlaps $Y_{ij}^{\gamma^\mu}(T)$ for $\mu = x$ between near-zero modes 1 and -1 that contribute to the disconnected piece of the flavor-singlet vector meson correlator at zero spatial momentum. Results are given for the average over $|Q| = 1$ configurations in the fine ensemble, set 5.

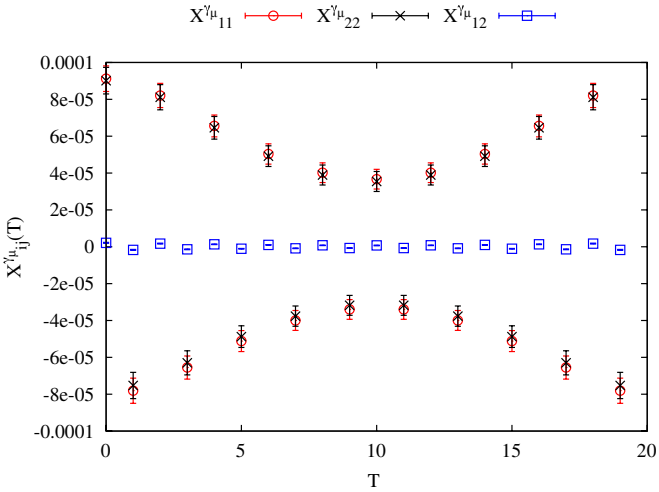

FIG. 21 (color online). The correlated overlaps $X_{ij}^{\gamma^\mu}(T)$ for $\mu = x$ between near-zero modes 1 and 2 that contribute to the disconnected piece of the flavor-singlet vector meson correlator at zero spatial momentum. Results are given for the average over $|Q| = 1$ configurations in the fine ensemble, set 5.

4. Summary

We conclude that the behavior of the staggered flavor-taste singlet meson correlators in every case follows that expected in continuum QCD. In particular, no chiral-limit divergence results from the near-zero modes. In all cases, we find that the Y_{ij}^{Γ} take the same average value for *i, j* both in a given quartet. Thus, the disconnected contribution from a quartet of degenerate eigenvalues is $4 \times 4 = 16$ times that of a single mode. The off-diagonal correlated overlaps X_{ij} are zero for *i, j* within a quartet in every case. This means that the connected contributions give instead 4 times that of a single mode. Including the factors of 4 and 16 in Eq. (49) means that the correlator is effectively made of single-species contributions, as in continuum QCD, and, in particular, the contribution from near-zero modes cancels as it does there.

The pseudoscalar and scalar cases are particularly simple to analyze, both for zero and nonzero modes, and to see the clear correspondence with continuum behavior. The correlated overlaps for the taste-singlet pseudoscalar between mirror quartets are a striking demonstration of how staggered fermions conspire to give the "right" answer, but sometimes in a rather nontrivial way. The match demonstrated between the taste-singlet and the Goldstone pseudoscalar also leads to a practical suggestion that may improve the determination of the η' mass using staggered fermions. The calculation of the taste-singlet connected and disconnected contributions is particularly statistically noisy because of the point-split nature of the taste-singlet operator. It may be preferable, although numerically challenging, to determine instead the near-zero-mode eigenvectors and then subtract their contribution from the Goldstone pseudoscalar correlator. This must agree with

the η' correlator in the continuum limit and yet is constructed of local operators and so has significantly less gauge noise.

V. CONCLUSIONS

This paper adds weight to the growing evidence that shows that staggered fermions behave in the correct way to reproduce QCD in the continuum limit, even with the rooted determinant. Here we have focused on the eigenvectors of the staggered-fermion Dirac operator and the way in which the 't Hooft vertex and flavor-singlet meson correlators are built from the overlaps between different eigenvectors, using the appropriate taste singlets. The important overlaps are those between eigenvectors within a near-zero quartet since these could have generated dangerous singular terms as $m \to 0$. From our theoretical results we determine a condition for the local overlaps that needs to hold and then test this numerically and demonstrate that it does. Indeed we see that the near-zero-mode quartet in all cases behaves functionally in such a way to reproduce the required behavior of four copies of a single mode that mimics the expected behavior in the continuum.

Most of our results are not surprising, but in providing a clear link between the theoretical requirements and the numerical results for the eigenvector overlaps, we add further confidence to the soundness of the framework for the accurate phenomenology that is being done with staggered fermions. We demonstrate most directly that a calculation of flavor-singlet meson masses, notably that of the η' meson, should give the correct QCD result. This is not a substitute for doing the full calculation and this is underway [31,32].

ACKNOWLEDGMENTS

We thank Alistair Hart for generating the configurations [27,30], and we thank Junko Shigemitsu for alerting us to Ref. [48]. This work was funded by STFC, the Scottish Universities Physics Alliance, MICINN (under Grants No. FPA2009-09638 and No. FPA2008-10732), DGIID-DGA (Grant No. 2007-E24/2), and by the EU under ITN-STRONGnet (PITN-GA-2009-239353). E. F. is supported by the MICINN Ramón y Cajal program. Fermilab is operated by Fermi Research Alliance, LLC, under Contract No. DE-AC02-07CH11359 with the United States Department of Energy. The calculations were performed at the High Performance Computing Centre in Cambridge as part of the DiRAC facility, jointly funded by STFC, the Large Facilities Capital Fund of BIS, and the Universities of Cambridge and Glasgow.

APPENDIX A: DETAILED FORMULAS

For Sec. IV C it is convenient to spread staggered-fermion bilinears over a hypercube, inserting the lattice gauge field to preserve gauge invariance. An explicit construction is

$$S_I(x) = \frac{1}{16}\sum_b \bar{\chi}(x+b)\chi(x+b), \tag{A1}$$

$$V_I^\mu(x) = \frac{i}{16}\sum_b \eta^\mu(x+b)\bar{\chi}(x+\bar{b}^{(\mu)}) \times U(x+\bar{b}^{(\mu)}, x+b)\chi(x+b), \tag{A2}$$

$$T_I^{\mu\nu}(x) = -\frac{1}{16}\sum_b \eta^\mu(x+\bar{b}^{(\mu\nu)})\eta^\nu(x+b)\bar{\chi}(x+\bar{b}^{(\mu\nu)}) \times \bar{U}(x+\bar{b}^{(\mu\nu)}, x+b)\chi(x+b),\ \nu \neq \mu, \tag{A3}$$

$$A_I^\mu(x) = \frac{i}{16}\sum_b \eta^\mu(x+d-\bar{b}^{(\mu)})\eta_1(x+b)\eta_2(x+b) \times \eta_3(x+b)\eta_4(x+b)\bar{\chi}(x+d-\bar{b}^{(\mu)}) \times \bar{U}(x+d-\bar{b}^{(\mu)}, x+b)\chi(x+b), \tag{A4}$$

$$P_I(x) = \frac{1}{16}\sum_b \eta_1(x+b)\eta_2(x+b)\eta_3(x+b)\eta_4(x+b) \times \bar{\chi}(x+d-b)\bar{U}(x+d-b, x+b)\chi(x+b), \tag{A5}$$

where b runs over the 2^4-site hypercube with origin x; $\bar{b}_\mu^{(\mu)} = a - b_\mu$ but $\bar{b}_\rho^{(\mu)} = b_\rho$, $\rho \neq \mu$; $\bar{b}_\lambda^{(\mu\nu)} = a - b_\lambda$, $\lambda = \mu, \nu$, but $\bar{b}_\rho^{(\mu\nu)} = b_\rho$, $\rho \neq \mu, \nu$; and $d = (\hat{1}+\hat{2}+\hat{3}+\hat{4})a$. Gauge invariance is ensured via averages of parallel transport over paths from x to x', $\bar{U}(x, x')$.[2] Under shift symmetry these are all taste singlets. The vector current and scalar density satisfy the Ward identity corresponding to quark-number conservation for all a, and the axial-vector and pseudoscalar density satisfy the anomalous Ward identity as $a \to 0$. In practice, we use in place of U the HISQ-smeared gauge field W, defined in Eq. (B5) below.

For brevity and clarity, it is then helpful to write

$$S_I(x) = \bar{\chi}1_I\chi, \tag{A6}$$

$$V_I^\mu(x) = i\bar{\chi}\gamma_I^\mu\chi, \tag{A7}$$

$$T_I^{\mu\nu}(x) = \bar{\chi}i\sigma_I^{\mu\nu}\chi, \tag{A8}$$

$$A_I^\mu(x) = i\bar{\chi}\gamma_I^{\mu 5}\chi, \tag{A9}$$

$$P_I(x) = \bar{\chi}\gamma_I^5\chi, \tag{A10}$$

[2]There is no bar on $U(x+\bar{b}^{(\mu)}, x+b)$ because only the one-link path enters.

which with Eqs. (A1)–(A5) *define* 1_I, γ_I^μ, $i\sigma_I^{\mu\nu}$, $\gamma_I^{\mu 5}$, and γ_I^5, when acting on χ, $\bar{\chi}$, and the eigenvectors of $D_{\rm stag}$ for the analysis of ζ_{ij}^Γ in Sec. IV C.

When constructing the correlators for the η' and other flavor-taste-singlet correlators, it is more customary to restrict the operators to one time slice. In Sec. IV D 1, therefore, we average over spatial cubes only [and then time slices, cf. Eqs. (46)]. V_I^4 and $\boldsymbol{A}_I$ remain as in Eqs. (A2)–(A4), because they naturally extend over a time-like link or three-dimensional cube. For P_I, the operator is defined as attached to point on a time slice by averaging over all hypercubes that have a corner at that point, i.e. extending both forwards and backwards in time. Then averaging over a time slice is straightforward.

APPENDIX B: IMPROVED STAGGERED ACTIONS

To introduce improved staggered-fermion actions, it is convenient to proceed in steps, introducing notation along the way. The first step is "Fat7" smearing [72],

$$\mathcal{F}_\mu U_\mu = \prod_{\rho\neq\mu}^{\rm sym}\left[1+\frac{1}{4}(T_\rho + T_{-\rho} - 2)\right]U_\mu, \tag{B1}$$

which yields paths of length 3, 5, and 7. Here $T_{\pm\rho}U_\mu(x) = U_{\pm\rho}(x)U_\mu(x\pm\hat{\rho}a)U_{\mp\rho}(x\pm\hat{\rho}a)$, $U_{-\rho}(x) = U_\rho^\dagger(x-\hat{\rho}a)$. It is easy to check that the smearing introduces a form factor that reduces the coupling to taste-changing gluons [69].

As is often the case with smearing algorithms, Fat7 smearing introduces additional discretization errors. These can be removed by introducing an order-a^2 improvement [73]

$$V_\mu = (\mathcal{F}_\mu - \tfrac{1}{4}\mathcal{L}_\mu)U_\mu, \tag{B2}$$

where

$$\mathcal{L}_\mu U_\mu = \sum_{\rho\neq\mu}(T_\rho - T_{-\rho})^2 U_\mu \tag{B3}$$

introduces the five-link Lepage term. The discretization error of the simple difference operator in Eq. (3) can be removed with the three-link Naik term [70],

$$S_{\rm Naik} = -\frac{1}{12}a^3\sum_{x,\mu}\eta_\mu(x)\bar{\chi}(x)(T_\mu - T_{-\mu})^3\chi(x), \tag{B4}$$

where now $T_{\pm\mu}\chi(x) = U_{\pm\mu}(x)\chi(x\pm\hat{\mu}a)$.

For the HISQ action, Fat7 smearing is applied twice, with the Lepage correction taken at the second step

$$W_\mu = (\mathcal{F}_\mu - \tfrac{1}{2}\mathcal{L}_\mu)\mathcal{U}\mathcal{F}_\mu U_\mu, \tag{B5}$$

where $\mathcal{U}$ denotes a reunitarization and projection to SU(3). [The SU(3) projection makes little difference in practice.] The HISQ action is then

$$S_{\rm HISQ} = S_{\rm stag}(W_\mu) + S_{\rm Naik}(\mathcal{U}\mathcal{F}_\mu U_\mu), \tag{B6}$$

substituting for the original gauge field U_μ as shown.

For completeness we write the Fat7 × Asqtad [30] and Asqtad [73] actions in this notation:

$$S_{\rm Fat7\times Asqtad} = S_{\rm stag}(\check{W}_\mu) + S_{\rm Naik}(\mathcal{U}\mathcal{F}_\mu U_\mu), \tag{B7}$$

$$\check{W}_\mu = (\mathcal{F}_\mu - \tfrac{1}{4}\mathcal{L}_\mu)\mathcal{U}\mathcal{F}_\mu U_\mu, \tag{B8}$$

$$S_{\rm Asqtad} = S_{\rm stag}(V_\mu) + S_{\rm Naik}(U_\mu). \tag{B9}$$

Unfortunately, Ref. [27] referred to Fat7 × Asqtad as "HISQ." The Asqtad action defines the rooted determinant in the MILC ensembles [11,26], which have been used by the zero-temperature results cited in the Introduction. For this action there is an additional tadpole-improvement step in which one replaces $T_{\pm\rho}\chi$ and $T_{\pm\rho}U_\mu$ by $u_0^{-1}T_{\pm\rho}\chi$ and $u_0^{-2}T_{\pm\rho}U_\mu$, respectively, where u_0 is a measure of the mean link. In MILC's simulations of the Asqtad action [11], u_0 is set by the fourth root of the 1×1 Wilson loop (the plaquette). (The reunitarization in HISQ makes tadpole improvement unnecessary).

APPENDIX C: FURTHER REMARKS ON REFS. [35,36]

Creutz [35,36] makes several remarks that sound simple, and thus seem to be accepted by nonexperts, but they do not withstand careful scrutiny. One, explained elsewhere [19], is that the different tastes have different chirality. As discussed above, all near-zero modes within a common quartet possess (identically for mirrors; empirically otherwise) the same taste-singlet chirality, Eqs. (25) or (26). The nonzero modes all have (nearly) zero taste-singlet chirality. Finally, all modes have no net Goldstone chirality, $\sum_x f_s(x)\gamma_P^5 f_s(x) = \sum_x \varepsilon(x) f_s(x) f_s(x) = \sum_x f_{-s}(x) f_s(x) = 0$.

Another incorrect statement [36] concerns the θ angle of the strong CP problem, which can appear via a modified mass term

$$m\bar{\psi}\psi \mapsto m\cos(\theta)\bar{\psi}\psi + im\sin(\theta)\bar{\psi}\gamma_5\psi. \tag{C1}$$

Creutz states correctly that θ obtains a physical meaning via the anomaly and, hence, the ultraviolet regulator. He also states, incorrectly, that staggered fermions cannot possess this property, owing to the exact U_ε symmetry.

With this symmetry, the following two mass terms are, of course, equivalent:

$$m\bar{\chi}\chi(x) \leftrightarrow m\cos(\varphi)\bar{\chi}\chi(x) + im\sin(\varphi)\varepsilon(x)\bar{\chi}\chi(x). \tag{C2}$$

In the continuum limit, however, this corresponds to

$$m\bar{q}q(x) \leftrightarrow m\cos(\varphi)\bar{q}q(x) + im\sin(\varphi)\bar{q}\gamma_5\xi_5 q(x), \tag{C3}$$

namely is a taste *nonsinglet*. It is superficially the kind of transformation used to set up twisted-mass Wilson fermions [76], but we have seen no argument that proves it is the

same. In particular, unlike the unsubstantiated mass terms posited in Refs. [59,60], $\varepsilon(x) = \sum_s f_s(x) f^\dagger_{-s}(x)$ is *off-diagonal* in any basis where Eq. (13) makes sense.

The correct analog of Eq. (C1) is

$$m\bar{\chi}\chi \mapsto (x) m\bar{\chi}[\cos(\theta) + i\sin(\theta)\gamma_I^5]\chi(x). \tag{C4}$$

The taste singlet γ_I^5 extends across a hypercube and depends on the lattice gauge field. It thus relies on the regulator for its definition, as it must. To simulate the θ vacuum via the fermion mass, one needs to implement Eq. (C4), not Eq. (C2) [25,62].

[1] C. T. H. Davies *et al.* (HPQCD, MILC, and Fermilab Lattice Collaborations), Phys. Rev. Lett. **92**, 022001 (2004).
[2] C. Aubin *et al.* (Fermilab Lattice, MILC, and HPQCD Collaborations), Phys. Rev. Lett. **95**, 122002 (2005).
[3] C. Aubin *et al.* (Fermilab Lattice, MILC, and HPQCD Collaborations), Phys. Rev. Lett. **94**, 011601 (2005).
[4] I. F. Allison *et al.* (HPQCD and Fermilab Lattice Collaborations), Phys. Rev. Lett. **94**, 172001 (2005).
[5] A. Gray *et al.*, Phys. Rev. D **72**, 094507 (2005).
[6] Y. Aoki, G. Endrődi, Z. Fodor, S. D. Katz, and K. K. Szabó, Nature (London) **443**, 675 (2006).
[7] C. T. H. Davies *et al.* (HPQCD Collaboration), Phys. Rev. D **78**, 114507 (2008).
[8] C. T. H. Davies *et al.* (HPQCD Collaboration), Phys. Rev. Lett. **104**, 132003 (2010).
[9] C. T. H. Davies *et al.* (HPQCD Collaboration), Phys. Rev. D **82**, 114504 (2010).
[10] H. Na, C. T. H. Davies, E. Follana, G. P. Lepage, and J. Shigemitsu (HPQCD Collaboration), Phys. Rev. D **82**, 114506 (2010).
[11] A. Bazavov *et al.*, Rev. Mod. Phys. **82**, 1349 (2010).
[12] A. S. Kronfeld, arXiv:1007.1444.
[13] L. Susskind, Phys. Rev. D **16**, 3031 (1977).
[14] H. S. Sharatchandra, H. J. Thun, and P. Weisz, Nucl. Phys. **B192**, 205 (1981).
[15] K. Jansen, Proc. Sci., LATTICE2008 (2008) 010 [arXiv:0810.5634].
[16] H. W. Hamber, E. Marinari, G. Parisi, and C. Rebbi, Phys. Lett. **124B**, 99 (1983).
[17] S. Dürr, Proc. Sci., LAT2005 (2006) 021 [arXiv:hep-lat/0509026].
[18] S. R. Sharpe, Proc. Sci., LAT2006 (2006) 022 [arXiv:hep-lat/0610094].
[19] A. S. Kronfeld, Proc. Sci., LAT2007 (2007) 016 [arXiv:0711.0699].
[20] M. Golterman, Proc. Sci., CONFINEMENT8 (2008) 014 [arXiv:0812.3110].
[21] D. H. Adams, Phys. Rev. Lett. **92**, 162002 (2004).
[22] D. H. Adams, Nucl. Phys. Proc. Suppl. **140**, 148 (2005).
[23] D. H. Adams, Phys. Rev. D **72**, 114512 (2005).
[24] S. Dürr and C. Hoelbling, Phys. Rev. D **71**, 054501 (2005).
[25] S. Dürr and C. Hoelbling, Phys. Rev. D **74**, 014513 (2006).
[26] C. Aubin *et al.* (MILC Collaboration), Phys. Rev. D **70**, 114501 (2004).
[27] E. Follana, A. Hart, and C. T. H. Davies (HPQCD Collaboration), Phys. Rev. Lett. **93**, 241601 (2004).
[28] S. Dürr, C. Hoelbling, and U. Wenger, Phys. Rev. D **70**, 094502 (2004).
[29] K. Y. Wong and R. M. Woloshyn, Phys. Rev. D **71**, 094508 (2005).
[30] E. Follana, A. Hart, C. T. H. Davies, and Q. Mason (HPQCD Collaboration), Phys. Rev. D **72**, 054501 (2005).
[31] E. B. Gregory, A. C. Irving, C. M. Richards, and C. McNeile, Phys. Rev. D **77**, 065019 (2008).
[32] E. B. Gregory *et al.*, at Lattice 2011 [https://latt11.llnl.gov/].
[33] K. Jansen, C. Michael, and C. Urbach (ETM Collaboration), Eur. Phys. J. C **58**, 261 (2008).
[34] N. H. Christ *et al.* (RBC and UKQCD Collaborations), Phys. Rev. Lett. **105**, 241601 (2010).
[35] M. Creutz, Proc. Sci., LAT2007 (2007) 007 [arXiv:0708.1295].
[36] M. Creutz, Proc. Sci., CONFINEMENT8 (2008) 016 [arXiv:0810.4526].
[37] G. 't Hooft, Phys. Rev. Lett. **37**, 8 (1976).
[38] G. 't Hooft, Phys. Rev. D **14**, 3432 (1976).
[39] L. Venkataraman and G. Kilcup, arXiv:hep-lat/9711006.
[40] C. Bernard, M. Golterman, Y. Shamir, and S. R. Sharpe, Phys. Lett. B **649**, 235 (2007).
[41] C. Bernard, M. Golterman, Y. Shamir, and S. R. Sharpe, Phys. Rev. D **77**, 114504 (2008).
[42] E. Eichten and J. Preskill, Nucl. Phys. **B268**, 179 (1986).
[43] L. H. Karsten and J. Smit, Nucl. Phys. **B183**, 103 (1981).
[44] J. Smit and J. C. Vink, Nucl. Phys. **B298**, 557 (1988).
[45] M. F. L. Golterman, Nucl. Phys. **B273**, 663 (1986).
[46] G. W. Kilcup and S. R. Sharpe, Nucl. Phys. **B283**, 493 (1987).
[47] W.-J. Lee and S. R. Sharpe, Phys. Rev. D **60**, 114503 (1999).
[48] G. P. Lepage (unpublished).
[49] F. Gliozzi, Nucl. Phys. **B204**, 419 (1982).
[50] H. Kluberg-Stern, A. Morel, O. Napoly, and B. Petersson, Nucl. Phys. **B220**, 447 (1983).
[51] Y. Shamir, Phys. Rev. D **71**, 034509 (2005).
[52] Y. Shamir, Phys. Rev. D **75**, 054503 (2007).
[53] C. Bernard, M. Golterman, and Y. Shamir, Phys. Rev. D **73**, 114511 (2006).
[54] B. Bunk, M. Della Morte, K. Jansen, and F. Knechtli, Nucl. Phys. **B697**, 343 (2004).
[55] A. Hart and E. Müller, Phys. Rev. D **70**, 057502 (2004).
[56] M. F. Atiyah and I. M. Singer, Bull. Am. Math. Soc. **69**, 422 (1963).
[57] M. F. Atiyah and I. M. Singer, Ann. Math. **87**, 546 (1968).

[58] M. Creutz, Ann. Phys. (N.Y.) **323**, 2349 (2008).
[59] M. Creutz, Proc. Sci., QCD-TNT09 (2009) 008 [arXiv:1103.3304].
[60] M. Creutz, Acta Phys. Slovaca **61**, 1 (2011).
[61] D. H. Adams, Phys. Rev. Lett. **104**, 141602 (2010).
[62] J. C. Vink, Phys. Lett. B **210**, 211 (1988).
[63] E. Follana *et al.* (HPQCD Collaboration), Phys. Rev. D **75**, 054502 (2007).
[64] M. Creutz, Phys. Rev. D **78**, 078501 (2008).
[65] C. Bernard, M. Golterman, Y. Shamir, and S. R. Sharpe, Phys. Rev. D **78**, 078502 (2008).
[66] P. Weisz, Nucl. Phys. **B212**, 1 (1983).
[67] G. P. Lepage and P. B. Mackenzie, Phys. Rev. D **48**, 2250 (1993).
[68] J. B. Zhang *et al.*, Phys. Rev. D **65**, 074510 (2002).
[69] G. P. Lepage, in *Perturbative and Nonperturbative Aspects of Quantum Field Theory*, edited by H. Latal and W. Schweiger (Springer-Verlag, Berlin, 1997).
[70] S. Naik, Nucl. Phys. **B316**, 238 (1989).
[71] J. F. Lagaë and D. K. Sinclair, Phys. Rev. D **59**, 014511 (1998).
[72] K. Orginos, D. Toussaint, and R. L. Sugar (MILC Collaboration), Phys. Rev. D **60**, 054503 (1999).
[73] G. P. Lepage, Phys. Rev. D **59**, 074502 (1999).
[74] E. Follana, C. T. H. Davies, G. P. Lepage, and J. Shigemitsu (HPQCD Collaboration), Phys. Rev. Lett. **100**, 062002 (2008).
[75] A. Bazavov *et al.* (MILC Collaboration), Phys. Rev. D **82**, 074501 (2010).
[76] R. Frezzotti, Nucl. Phys. Proc. Suppl. **140**, 134 (2005).